

8-2018

Nonlinear Acoustic Waves Generated by Surface Disturbances and Their Effect on Lower Thermospheric Composition

Benedict Piñeyro

Follow this and additional works at: <https://commons.erau.edu/edt>



Part of the [Engineering Physics Commons](#)

Scholarly Commons Citation

Piñeyro, Benedict, "Nonlinear Acoustic Waves Generated by Surface Disturbances and Their Effect on Lower Thermospheric Composition" (2018). *Dissertations and Theses*. 414.
<https://commons.erau.edu/edt/414>

This Thesis - Open Access is brought to you for free and open access by Scholarly Commons. It has been accepted for inclusion in Dissertations and Theses by an authorized administrator of Scholarly Commons. For more information, please contact commons@erau.edu.

NONLINEAR ACOUSTIC WAVES GENERATED BY SURFACE
DISTURBANCES AND THEIR EFFECTS ON LOWER
THERMOSPHERIC COMPOSITION

BY
BENEDICT PIÑEYRO

A Thesis

Submitted to the Department of Physical Sciences
and the Committee on Graduate Studies
In partial fulfillment of the requirements
for the degree of
Master in Science in Engineering Physics

08/2018

Embry-Riddle Aeronautical University
Daytona Beach, Florida

© Copyright by Benedict Piñeyro 2018
All Rights Reserved


NONLINEAR ACOUSTIC WAVES GENERATED BY SURFACE
DISTURBANCES AND THEIR EFFECTS ON LOWER
THERMOSPHERIC COMPOSITION

by

Benedict Piñeyro

This thesis was prepared under the direction of the candidate's Thesis Committee Chair, Dr. Jonathan B. Snively, Associate Professor, Daytona Beach Campus, and Thesis Committee Members Dr. Michael Hickey, Associate Professor, Daytona Beach Campus, and Dr. Roberto Sabatini, Research Associate, Daytona Beach Campus, and has been approved by the Thesis Committee. It was submitted to the Department of Physical Sciences in partial fulfillment of the requirements of the degree of Master of Science in Engineering Physics

THESIS COMMITTEE:



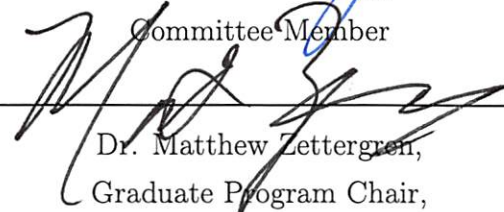
Dr. Jonathan B. Snively,
Committee Chair



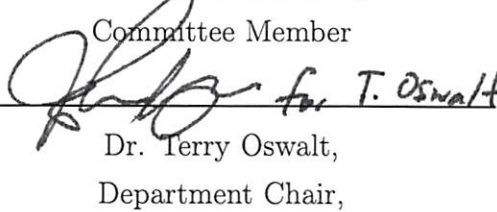
Dr. Michael Hickey,
Committee Member



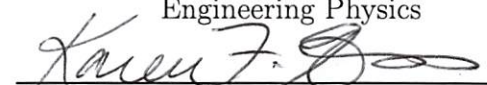
Dr. Roberto Sabatini,
Committee Member




Dr. Matthew Zettergren,
Graduate Program Chair,
Engineering Physics



Dr. Terry Oswald,
Department Chair,
Physical Sciences



Dr. Karen Gaines,
Dean, College of Arts and Sciences



Lon D. Moeller,
Senior V.P. for Academic Affairs

Abstract

Recent nonlinear atmospheric models have provided important insight into acoustic waves generated by seismic events, which may steepen into shocks or saw-tooth trains while also dissipating strongly in the thermosphere. Although they have yielded results that agree with observations of ionospheric perturbations, dynamical models for the diffusive and stratified lower thermosphere often use single gas approximations with height-dependent physical properties (e.g. mean molecular weight, specific heats) that do not vary with time (fixed composition). This approximation is simpler and less computationally expensive than a true multi-fluid model, yet captures the important physical transition between molecular and atomic gases in the lower thermosphere. Models with time-dependent composition and properties have been shown to outperform commonly used models with fixed properties; these time-dependent effects have been included in a one-gas model by adding an advection equation for the molecular weight, finding closer agreement to a true binary-gas model (e.g. Walterscheid and Hickey [2012]).

Here, a one-dimensional nonlinear mass fraction approach to multi-constituent gas modeling, motivated by the results of Walterscheid and Hickey, is presented. A flux-differencing finite volume method is implemented in Clawpack with a Riemann Solver to solve the Euler Equations including multiple species, defined by their mass fractions, as they undergo advection. Viscous dissipation and thermal conduction are applied via a fractional step method. The model is validated with shock tube problems for two species, and then applied to investigate propagating nonlinear acoustic waves from ground to thermosphere, such as following the 2011 Tohoku Earthquake

and rocket launches. The limits of applicability are investigated for vertically propagating acoustic waves near the cut-off frequency, and for simulations of steepening waves at finite spatial resolution. The addition of a mass fraction density introduce noticeable fluctuations to the state of the atmosphere that can account for modulation of acoustic waves. The model developed also has potential uses in parametric studies, complementing more costly 2D and 3D models.

Acknowledgments

I would like to thank my advisor, Dr. Jonathan B. Snively, for his guidance and support during my undergrad and Master's. Without his influence, the work presented before you would not be possible. I would also like to thank my thesis committee, Dr. Michael Hickey, Dr. Roberto Sabatini, and Dr. Matthew Zettergren for their feedback on my research.

I'm also extremely thankful for my family who gave me limitless support and love. To my mother, Maria E. Piñeyro, my sister Melina Piñeyro, and my father Bienvenido Piñeyro, thank you for being a part of my life.

Finally, I would like to thank Lisa Cesaroni, and my friends in the ECLAIR lab, Pavel Inchin, Fan Yang, and Dr. Chris Heale for their support.

Contents

Abstract	iv
Acknowledgments	vi
1 INTRODUCTION	1
1.1 Scientific Background	1
1.1.1 Standard Atmosphere	1
1.1.2 Literature Review	4
1.1.3 Acoustic Wave Observations	5
1.1.4 Acoustic Wave Models	9
1.1.5 Problem Formulation	13
1.1.6 Organization of the Thesis	13
2 MATHEMATICAL MODEL	15
2.1 Physical and Mathematical Basis	16
2.1.1 Stratified Atmosphere	16
2.1.2 Euler Equations	19
2.1.3 Linear Dispersion	20
2.1.4 Viscous Diffusion and Thermal Conduction	23
2.1.5 Chapter Summary	28
3 NUMERICAL MODEL IMPLEMENTATION	29
3.1 Finite Volume Methods	30
3.1.1 Godunov’s Wave-Propagation Method	31

3.1.2	Methods for Parabolic Equations	34
3.1.3	Mass-Fraction Density	38
3.1.4	Multi-dimensional Symmetry	41
3.1.5	Riemann Solver Validation	42
3.1.6	Chapter Summary	48
4	INVESTIGATIONS OF PARAMETER EFFECTS	49
4.1	Model Applicability and Extent	49
4.1.1	Tohoku Earthquake	50
4.1.2	Mabie et al. Rocket Launch	54
4.1.3	Misty Picture Experiment	57
4.2	Effects of Compositional Variation	60
4.3	Chapter Summary	65
5	SUMMARY AND SUGGESTIONS FOR FUTURE WORK	66
5.1	Summary	66
5.2	Conclusion	66
5.3	Future Work	68
5.3.1	Parametric Resonance Study	68
5.3.2	Future Model Additions	70
A	DERIVATIONS	A – 1
A.1	Jacobian: Euler Equations	A – 1

List of Tables

2.1	Tables of the major atmospheric constituents and their fit parameters for thermal conductivity and viscosity obtained from Rees [1989] . . .	27
3.1	Sod test simulation parameters for Riemann problem validation . . .	45
4.1	Table of parameters and source characteristics for the Tohoku, or Zettergren et al. [2017] case study	51
4.2	Table of parameters and source characteristics for the 1D simulation for the acoustic wave observations reported by Mabie et al. [2016] . .	55
4.3	Table of source characteristics for the Misty Picture Experiment . . .	58

List of Figures

1.1	The atmosphere's major constituents number density variations (left) and temperature variations with altitude. The layers are defined through regions of a temperature gradient equal to zero, or through a sign change from previous layer. The profile was obtained from NRLMSISE-00 Picone et al. [2002].	3
2.1	The atmosphere's density and pressure with altitude (left) and the temperature and speed of sound with altitude (right).	17
2.2	The mean molecular weight (left), mass fraction density (center), and the specific heat ratio and specific gas constant (right) as a function of altitude.	18
2.3	Dispersion curves for wave propagation in a compressible, gravitationally stratified medium for a given height in the atmosphere. Image adopted from Vigeesh et al. [2017] and Gossard and Hooke [1975]. . .	22
2.4	The empirical dynamic viscosity and thermal conductivity derived in Rees [1989] with altitude (left). The Prandtl number (right) is defined as the ratio of thermal diffusivity to kinematic viscosity.	26
3.1	A grid perspective of a finite volume cell with a left and right flux going into (and out of) it.	30
3.2	Gravity as calculated by Newton's law (black) and calculated using NRLMSISE-00 atmospheric properties with hydrostatic equilibrium. .	35
3.3	A grid used in a one dimensional finite difference method (left) and the progression of the discretized diffusion values (right).	36

3.4	One-dimensional Sod test with initial conditions ($t = 0$) and after some time t_s . After $t = 0$, the diaphragm is ruptured and the gas with higher pressure q_L expands to the region of lower pressure q_R	43
3.5	Sod test with shock wave and contact discontinuity labeled as white lines and calculated from the analytical solution. The results for initial conditions in Table 3.1 are shown in the left, while the reverse of Table 3.1 are shown on the right.	46
3.6	Parameters from the Sod test with the conditions found in Table 3.1, when atomic oxygen begins on the left.	47
3.7	Parameters from the Sod test with the conditions found in Table 3.1, but q_L and q_R are reversed, when atomic oxygen begins on the left.	47
4.1	The acoustic Mach number (top right), speed of sound (top left), atomic oxygen mass fraction density (bottom left), and atomic oxygen in log scale (bottom right).	52
4.2	The velocity profile of a one-dimensional simulation of the Tohoku Earthquake as done by Zettergren et al. [2017] compared to the results of the 1D mass fraction density simulation (right).	53
4.3	The variation in the acoustic cutoff frequency ω_A [rad/s] (left) and the specific heat ratio (right) due to the mass-fraction density model.	54
4.4	Velocity profiles as inspired by Mabie et al. [2016] observation of a rocket launch with the use of the 1D model (right) compared to the 2D (left) version of the MAGIC model.	56
4.5	Velocity profiles as inspired by Mabie et al. [2016] observation of a rocket launch using 1D Mass Fraction Model (dashed) and the 2D/3D magic Cylindrical Simulation (solid), showing reasonable agreement.	57
4.6	Results of nonlinear Misty Picture run from Sabatini et al. [2016] (dark solid line) with the results of the 1D mass fraction density model with (dashed grey line) compositional variation superimposed with the same scale. The solid slate grey line (c) shows a run with no compositional variation.	59

4.7	Temporal signal at 90km (a) and the One-Sided energy spectral density obtained at different spatial resolutions (b). The plot shows reasonable agreement with Figure 16 in Sabatini et al. [2016].	60
4.8	Speed of sound perturbations from a source similar to the 2011 Tohoku simulation at three heights. The dashed and solid lines represent the speed of sound calculated with and without specific heat ratio variation respectively.	61
4.9	Velocity of acoustic wave for the simulation inspired by the results of Mabie et al. [2016]. The dashed lines are with compositional variation and the solid lines are without. The top shows the run with parameters from Table 4.2, and the bottom shows the same run with a source amplitude of ten times the one of the top run.	63
4.10	The Rocket Launch run with ten times the source amplitude as the parameters in Table 4.2. The difference between the varying specific heat ratio and the profile when the specific heat is constant.	64
4.11	Results of misty picture run with the same parameters from Table 4.3, but with a resolution of $\Delta z = 100\text{m}$. Sabatini et al. [2016] run is shown in (dark solid line) with the results of the 1D mass-fraction density with compositional variation (dashed gray line) and without variation (dashed black line).	65
5.1	An example of a potential parametric study that changes the frequency and envelope of a source to provide insight into spectral characteristics of unknown sources.	69

Chapter 1

INTRODUCTION

1.1 Scientific Background

This chapter contains a review of important literature and introductory material that provide basis for this thesis. The behavior of acoustic waves that propagate through transition regions in the atmosphere depend on composition. Studies on acoustic wave generation and their characterization are shown. This chapter's conclusion outlines the content of chapters that follow, and describes the contributions of this thesis.

1.1.1 Standard Atmosphere

Earth's atmosphere consists of four layers defined by variations of temperature with altitude: the troposphere, stratosphere, mesosphere, and thermosphere separated by the tropopause, stratopause, and mesopause respectively. The atmosphere's stratification contributes to vertically varying atmospheric properties, e.g. variations of the near exponential decay of pressure and density with altitude, which also influences atmospheric wave propagation. To understand the effects of vertical variations of the atmosphere on wave propagation, the layers will be described.

Troposphere

The bottom-most layer of Earth's atmosphere is the troposphere, that extends from the ground to around 10-20 kilometers. This is the densest region of the atmosphere, containing roughly four-fifths of the mass and 99% of the water vapor. This region is characterized by a temperature gradient that decreases at a rate of about 8.5 K/m. As a result of the water vapor and temperature variations, most of the weather occurs in this region. Natural processes and extreme weather may create acoustic or gravity waves in this region that propagate upwards.

Stratosphere

The stratosphere is above the troposphere, is bounded at the bottom by the tropopause and at the top by the stratopause, and extends between 20-50 kilometers. This region holds about 20% of the atmosphere's mass. The temperature and its gradient increases with altitude due to the absorption of solar radiation. Ultraviolet light breaks down oxygen into atomic oxygen and recombines with oxygen molecules to create the ozone layer. An increase in temperature gradient results in an increase in stability such that atmospheric waves can easily perturb the middle stratosphere region.

Mesosphere

The mesosphere (altitude range: 50-85 kilometers), similar to the troposphere, has a negative temperature gradient, but is rarefied compared to the layers below. At the top of the mesosphere, the ionosphere begins as electron and ion densities increase. The mesopause transition region of the upper mesosphere and the lower thermosphere is where atmospheric waves experience dramatic growth. The mesosphere has been difficult to study due to its altitude, but the mesopause is readily measured due to airglow and metal layers. As gravity waves reach the mesopause, they are often responsible for significant turbulence due to energy dissipation, and acceleration of flows due to their momentum flux.

Thermosphere

The most rarefied of the five layers is the thermosphere, which is located above the mesopause (around 90 kilometers). The temperature increases in this region due to solar radiation, and stabilizes in the exosphere. Similar to the upper mesosphere, it is

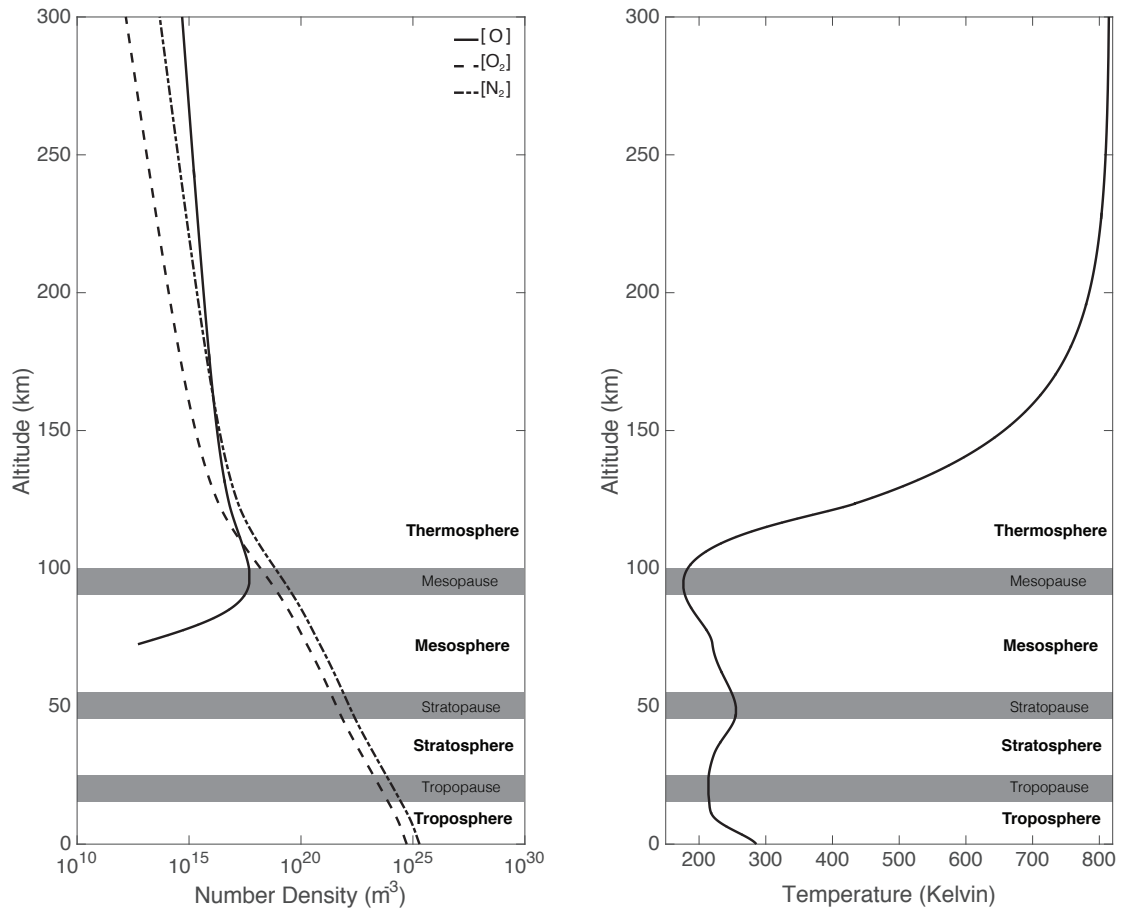


Figure 1.1: The atmosphere’s major constituents number density variations (left) and temperature variations with altitude. The layers are defined through regions of a temperature gradient equal to zero, or through a sign change from previous layer. The profile was obtained from NRLMSISE-00 Picone et al. [2002].

difficult to study the motion of the thermosphere without indirect measurements such as of ionospheric densities. Atmospheric waves have a significant contribution to the variability of atmospheric parameters. Waves with large scale (both horizontal and vertical) will often dominate the wind field in the mesosphere and lower thermosphere (MLT) [Vadas et al., 2003], and can often break, which produces body forces that drive large scale circulations and secondary waves [Vincent, 2015]. The lower thermosphere experiences vertical dynamical mixing in the transition region, and, due to the atmosphere's rarefaction, molecular diffusion produces gravitational separation of species. This thesis seeks to contribute to the modeling of acoustic waves at very low frequencies in this region – the mesosphere and lower thermosphere – as their composition varies dramatically with altitude.

1.1.2 Literature Review

Waves in the atmosphere have been studied indirectly by measurements and theory for over two hundred years. The early 1900s saw advancements in our understanding of atmospheric waves which resulted in the classification of the different types of atmospheric waves. The accessibility of instruments, maturity of theory, and advent of numerical models has resulted in considerable interest in the study of waves in the atmosphere, especially in the last fifty years. Current research areas include the attempt to identify signatures of large scale geophysical disturbances through atmospheric waves, and the investigation, via numerical models, of physical processes caused by waves in the atmosphere. Due to the large volume of work involved with waves in the atmosphere, this thesis will focus on acoustic waves only, excluding gravity waves. Atmospheric acoustics became more prominent along with measurements of infrasound in literature during the late 1960s after the invention of echosonde, or sodar along with measurements of infrasound Gossard and Hooke [1975]. Before the work of this thesis is outlined, it is relevant to include the work done in this branch of atmospheric waves, e.g. infrasonic acoustics, related to the work outlined in this thesis. The reader is encouraged to read Whitham [1999] and Pierce [1989] for more complete descriptions of nonlinear acoustic waves.

1.1.3 Acoustic Wave Observations

Acoustic waves can be generated in the atmosphere as a result of a number of sources, which are reviewed in this section to better understand the processes leading to vertically propagating acoustic waves. Infrasonic waves can occur due to man-made disturbances, such as nuclear detonations, and natural processes, such as severe storms and earthquakes. Ionospheric disturbances with time scales of acoustic waves have been measured over the past fifty years; Gossard and Hooke [1975] and McKisic [1997] are among those that have reviewed different sources for the purpose of infrasonic monitoring. Baker and Davies [1968] classified waves in the ionosphere that followed a nuclear detonation near Johnston and Christmas Islands in the Pacific and in Novaya Zemlya. The wave fluctuations were calculated from radio waves reflected from the $F2$ layer (at altitudes between 150-200 kilometers) measured with a 4,5 and 10MHz ionosonde, converting signal variations into changes of ionization and electron density. From the changes in ionization, they were able to deduce the group velocity of waves, which were compared to theoretical acoustic and gravity mode dispersion relations. Most of the observed waves with 30s - 10min periods were found to be in the acoustic domain. Their results supported Row [1966], who created a simple closed-form approximation of long-period pulse propagation in an isothermal stratified atmosphere. He applied his model to the Novaya Zemlya nuclear detonation and the 1964 Alaskan earthquake, which were interpreted with the use of similar techniques stated above. Row's findings offer an interpretation of the long-period oscillations data collected in the F -region, in the case of the nuclear detonations, but his model neglected important physical processes, such as the effects of viscosity and thermal conduction, which were known to play a role in theory.

Ionosonde data played an important role in the early establishment of acoustic-gravity wave measurements and their interpretations. The combination of theoretical predictions of group velocities compared to experimental data measured by Wickersham [1966] and King [1965] revealed fully ducted, acoustic-gravity modes where they were expected, but not previously observed. Wickersham [1966]'s work matched theoretical velocities with lower experimental velocities provided by Stoffregen [1962]. Kanellakos [1967] was able to match their theoretical-empirical formula

to the ionosonde data from various stations following the detonation of nuclear bomb test approximately 450 km southwest of Johnston Island to determine the influence of Earth's magnetic field on the interaction of a neutral acoustic-gravity wave, assumed horizontal travel, as it interacts with ionized constituents of the upper atmosphere. The latter paper formed much of its basis on the results of Hines [1960] and Hines [1965] that discussed the role of internal atmospheric gravity waves in heat transfer in the upper atmosphere.

Disturbances in the ionosphere measured by height variations in the phase of ionospherically reflected radio waves are also caused by singular, large scale surface events. Smaller more common disturbances, e.g. lightning, were also suspected as a source of ionospheric disturbances during the 1960s, with notable observations by Anderson [1960]. His observations were analyzed by Pierce and Coroniti [1966] who indicated the oscillations observed in storm cells should act as sources of waves. They predicted that waves with 10min periods would be produced. Years later, 3-5 minute periods wave trains were observed and Pierce and Coroniti [1966], concluded the frequency was doubled due to non-linear interactions in the source. Within the 3-10 minute period waves observed, only narrow bands were seen at high altitudes which was later given a qualitative explanation by Chimonas and Peltier [1974] as a result of interference of multiple reflections between the lower troposphere and the lower thermosphere.

Acoustic-gravity wave observations were first appreciated during the 1960s-1980s, confirming theoretical predictions with measurements based on measured ionospheric perturbations from ionosodes. Yeh and Liu [1974] provided a comprehensive, theoretical, review and characterization of the sources of acoustic-gravity waves based on their effects in the upper atmosphere. The sources of acoustic-gravity waves were sorted into: impulsive sources, sources due to seismic activity such as earthquakes, magnetic-storm related sources (e.g. displacement of supersonic auroral arcs due to the Lorentz Force), medium-scale disturbances due to mountain waves or severe storms, and short-period, (specifically infrasonic) disturbances, due to moving auroral jets. These categorizations come from observations reported in previous papers, such as a correlation between the high frequency Doppler recorder in Honolulu that

measured ionospheric perturbations at 300 kilometers, which was compared to seismograph data of a Rayleigh component of the seismic wave in Oahu, Hawaii. The time it took for the Rayleigh waves to arrive to Oahu at a predicted rate of 3.9 km/s with a 25 second period was compared to the time it took for the atmospheric disturbance to arrive to the Doppler recorder which matched well with the predicted value.

Yeh and Liu [1974] reviewed multiple methods of acoustic-gravity wave detection, and reported upper atmospheric heating due to acoustic-gravity waves, which was the focus of Hickey et al. [2001]. Hickey et al. [2001] conducted their study on acoustic waves revealing that persistent short period waves were primarily responsible for the heating of the upper thermosphere. Blanc [1985] also reviewed upper atmosphere disturbances related to energetic infrasonic sources, which include earthquakes, volcanic eruptions, polar aurora, convective storms, rocket launches, and powerful explosions. The characteristics of the waves depend on the source of the disturbance, for instance through vertical displacement of the ground displacements in the case of buried explosions. Although acoustic wave propagation in the atmosphere had its own theoretical studies, and observations (see Gossard and Hooke [1975] for an extensive list of early-known sources of infrasound), acoustic waves studies became more prevalent in the 1990s when the use of GPS data became a prominent medium of atmospheric wave detection.

Calais and Minster [1995] used GPS data gathered from the 1994 $M_w = 6.7$ Northridge earthquake to estimate fluctuations to ionospheric electron content. Data gathered from a GPS network is discussed in the terms of total electron content (TEC). They used the delayed radio broadcast signals of four GPS observables and converted the delayed signals in the ionosphere into TEC, and produced results that agreed well with numerical predictions, e.g. Davies and Archambeau [1994]. GPS arrays provide researchers with the opportunity to observe the source of an atmospheric wave, and the shock near, or above where the source originated. This allowed for more robust studies, leading to the development of theory and characterizations of acoustic waves in TEC. Afraimovich et al. [2000] used GPS data to investigate the

parameters of shock-acoustic waves generated during rocket launches. They developed an interferometric method to determine shock-acoustic wave parameters, such as phase velocity, that could determine the wave parameters without a priori information of the site and time of a rocket launch, as opposed to traditional radio-detection techniques. Several case studies were considered, e.g. SOYUZ rocket launches, and it was found that all of the general launches produced characteristic N -waves, with periods between $T = 270 - 360$ seconds, and amplitudes that exceeded the background TEC fluctuations. Previous publications had uncertain localization of the shock's region of generation, and varied definitions of fundamental parameters to define the shock acoustic wave, in the case of Karlov et al. [1980], and Nagorsky. [1998, 1999] who studied the Apollo mission launches. The ionospheric oscillation periods measured varied from 6 to 90 minute, and the propagation velocity was in the range of 600-1670 m/s, with several accompanied waves recorded after the first shock measurement. Afraimovich et al. [2000] identified shock-acoustic wave period in the range of 270-360 seconds, with wave vector angle of $35 - 60^\circ$, and a phase velocity of 900-1200 m/s which approaches the sound velocity at heights in the F -region which makes it possible to identify the sound nature of a TEC perturbation. GPS facilitated ionospheric observation that led Artru et al. [2004] to describe tsunami-induced gravity waves, which were predicted by Peltier and Hines [1976]. A continuation of Artru et al. [2005] led to an atmosphere-ocean coupled model which, when the ocean frequencies are above transition frequency, render acoustic-gravity waves that radiate their energy into the upper atmosphere. They concluded the acoustic-gravity waves of oceanic origin may have an observable impact on the upper atmosphere.

Contemporary measurements of atmospheric waves involve a combination of the aforementioned methods of detection as well as other remotely sensed sensors. Observations made with GRIPS (GRound-based Infrared P-Branch Spectrometers) allowed Le Pichon et al. [2013] to develop an automatic identification of spectral features and association to distinct infrasound sources based on airglow observation. These observations were validated for case studies of infrasonic waves of orographic origin (e.g. mountain associated waves), and due to volcanic and meteorological activity. The algorithm developed allowed several sources of infrasonic waves to be categorized based

on their amplitude at the mesopause region, and their period based on the airglow data. Farges et al. [2005] used a combination of cameras, and microbarometers to capture information on more than 130 sprites, to identify infrasound signals generated by sprites through simultaneous observation. Propagation times were estimated with use of a paraxial ray tracing model [Virieux et al., 2004]. Many acoustic wave observations come from a large-scale source and have limited instances of observation, whereas Le Pichon [2002] and Garces et al. [2004] characterized acoustic wave propagation and atmospheric characteristics based on a wide range of data. In the case of Le Pichon et al. [2005], they monitored active volcanoes in the Vanuatu archipelago and determined mesospheric zonal winds are underestimated in the range of 20-50m/s. Volcanic sources are unique since eruptions often involve a sudden, uncorked pressure release at the top of the volcano and hot gases and rock fragments are ejected incur acoustic or shock waves. Le Pichon [2002] compared the measurements of daily microbarograph data from France of supersonic Concorde flights between North America and Europe. The signals were used to investigate the effects of atmospheric variability on long-range sound propagation and compared to predictions obtained from theoretical ray path tracing in an atmospheric model; whose results include the ability to estimate wind velocity fluctuations at the reflection heights based on ground measurements.

The sources of atmospheric acoustic waves, and their effects on the atmosphere are not limited to the cases discussed above. For more material, the reader is encouraged to read comprehensive reviews, such as McKisic [1997] and Pichon et al. [2010].

1.1.4 Acoustic Wave Models

The nonlinear processes in the atmosphere challenge scientists and engineers to balance necessary computations, done through the simplification of mathematical models and inclusion of necessary physical processes, to produce solutions that agree with measured quantities at reasonable cost. However, there are some processes that are necessary to include numerical simulations of atmospheric waves, and the assumptions made depend on the region of the atmosphere in question and the type of processes

which are dominant. There are processes that are known to have minimal effects in the thermosphere such as eddy diffusion, ion drag, and the Coriolis force, that can be ignored for acoustic waves. Del Genio et al. [1978] showed wave-induced diffusion results in the phase and amplitude relationships between density fluctuations of individual atmospheric constituents to agree with AE-C satellite observations with a two-dimensional, two-gas, hydrostatic (isothermal), inviscid neutral atmosphere. As opposed to the observations of Dudis and Reber [1976] who studied acoustic-gravity waves in an isothermal atmosphere in diffusive equilibrium, but neglected the diffusive separation caused by the waves. Del Genio et al. [1978] results supported the notion that molecular diffusion above the turbopause prevented the atmosphere from being well-mixed which affects wave propagation.

Numerical models began to develop more after the 1990s. Hickey et al. [2001] proposed vertically propagating thermospheric acoustic waves, due to thunderstorms, could be the source of oscillations in the F -region. Walterscheid et al. [2003] reached a similar conclusion with their axisymmetric, f -plane, nonlinear, time-dependent numerical model, which they used to simulate acoustic waves in the mesosphere and thermosphere by intense deep convection in the troposphere. The implications of their work supports Hickey et al. [2001] conclusions, and the measurements made by Meriwether et al. [1996], who suggested acoustic waves might be responsible for the equatorial hot spot observed in airglow data over the Andes Mountains. Krasnov et al. [2007] conducted a parameteric study to determine when an acoustic wave, launched from Earth's surface, "broke". They found that the location of the "transformation zone", is inversely correlated to the acoustic wave frequency. The "transformation zone" absorbs a large part of the acoustic signal which contributes to the heating that has been detected and measured in that region.

Chum et al. [2016] highlighted the importance of nonlinear numerical simulations through a comparison of a linear and nonlinear numerical models of ionospheric fluctuations measured by continuous Doppler sounding at an altitude of 185 kilometers after a magnitude $M_w = 8.3$ earthquake offshore of the Coquimbo region of Chile in

2015. The measured vertical velocity of ground surface motion was used as boundary conditions in the system of compressible viscous fluid equations. The nonlinear numerical simulation of infrasound propagation explained the observed waveform with higher accuracy than the linear numerical model whenever the velocity of the air particles became comparable with the local sound speed. The role of nonlinear effects on the measured atmospheric response due to the earthquake was explored through the reduction of the initial perturbation (by 10^{-3}) which resulted in the absence of the N-shaped pulse. One-dimensional models, such as used by Chum et al. [2016], are valuable in their applicability to various case studies at low computational cost, at the expense of generality of geometry and assumptions about propagation. Direct numerical simulations of the two-dimensional unsteady, single-gas, compressible Navier-Stokes equations with thermoviscous effects included, were presented by Sabatini et al. [2016], using a high-order-finite-difference time-domain algorithm. The purpose was to study the long-range infrasound propagation through direct numerical simulation, including comparisons between linear and nonlinear sources which, like Chum et al. [2016], identified shock and N-wave formations in the upper atmosphere that correlated to the nonlinear sources. Molecular dissipation and nonlinearities are both increased by the decrease of the mean density with altitude.

Walterscheid and Hickey [2001, 2005] found vertically propagating acoustic waves can significantly contribute to thermospheric heating. Walterscheid and Hickey [2001] used a full-wave model to investigate whether dissipation of acoustic waves cools or heats the thermosphere. They found that vertically propagating acoustic waves can increase in scale from the mesosphere to the thermosphere and contribute significantly to the heating of the upper atmosphere. Walterscheid and Hickey [2005] used the same model used in Walterscheid and Hickey [2001] to examine acoustic wave generation by winds over hilly terrain. The results of their simulations could explain thermospheric hot spots near the Andes as reported by Meriwether et al. [1996].

Walterscheid and Hickey [2012] investigated gravity waves, where they imposed variations of compositional effects through the comparison of two one-gas full wave models: one where the molecular mass was fixed (fluctuations are zero), and the other where the molecular mass is conserved after parcel displacement. The gas models were

compared to a binary-gas model (mixture of atomic oxygen and molecular nitrogen). When the molecular mass is conserved, the results agreed with their binary-gas model which implied molecular mass variation contributes to the accuracy of the model. While acoustic waves at high frequencies do not meaningfully modulate composition, nonlinear acoustic waves at low frequencies can, which will be investigated in this thesis.

Zettergren et al. [2017] analyzed GPS-derived TEC to study the ionospheric response to infrasonic-acoustic waves caused by the 2011 Tohoku earthquake and tsunami. Their 2D simulations combined an ionospheric model, that captures chemical production and loss, and impact ionization with an atmospheric model, which solves for the neutral dynamics through the Euler equations coupled with solutions for molecular viscosity and thermal conduction. The neutral dynamics model is a variant of that used in Snively and Pasko [2008], which solved a similar set of equations for an inviscid atmosphere to describe thermally ducted wave modes in the lower thermosphere from a tropospheric source. Matsumara et al. [2011] had modeled the same earthquake and tsunami with a two-dimensional nonlinear neutral numerical model (with the basic state of the atmosphere derived from the NRLMSISE-00 empirical model) with an impulsive upward surface motion as the source of the perturbations. Although their source was weaker, they found dominant frequencies near the epicenter that indicated acoustic resonances between the ground-surface and lower thermosphere were excited by the earthquake. Thus, the ionospheric oscillations detected in the TEC were mainly due to the motion of the neutral atmosphere. Similar model simulations was reported in Zettergren and Snively [2013] and Zettergren and Snively [2015] also concluding that ionospheric signatures could provide insight into the forcing of the upper atmosphere from below, under a variety of sources and conditions. The 1D models developed in this thesis will be fully compatible with ones used previously by Zettergren and Snively [2015], but including additional physics.

1.1.5 Problem Formulation

This thesis is concerned with the development of a new approach that will be useful in modeling low frequency nonlinear acoustic waves while capturing the resulting modulation of the atmosphere. Interesting results can be achieved with linearized models, as shown above, however, nonlinear processes cannot be neglected as shown by Chum et al. [2016]. Other types of numerical approaches to atmospheric infrasonic propagation have been done, such as ray tracing, parabolic models, or normal mode theory which are beyond the scope of this thesis. Acoustic wave propagation, especially in the transition region between the mesosphere to the thermosphere remains a pertinent area of study, one this thesis seeks to make a contribution. A one-dimensional, nonlinear, mass fraction approach to multi-constituent gas modeling, motivated by the results of Walterscheid and Hickey [2001, 2012], that captures important physical transitions between molecular and atomic gases in the lower thermosphere is developed. The model will use NRLMSISE-00 as the basic state of the initial atmosphere and solves for perturbations made to it. It will be applied to a range of test cases for validation and to investigate modulation of composition and parameters.

1.1.6 Organization of the Thesis

Chapter 1 has served to introduce the reader to the literature relevant to the study of acoustic waves and to provide general background development. There is terminology that is developed in this chapter, which will be useful in later chapters, especially in the mathematical formulation of this study. Chapter 2 provides the theoretical basis of the thesis, and shows the equations that govern the gases in the atmosphere and introduces the mass-fraction density approach to be used. There are several assumptions that are made within this chapter which are necessary for their discrete treatment in a numerical model. Chapter 3 will discuss the discretization of the equations discussed in Chapter 2, with an emphasis on the implementation of CLAWPACK, and the various methods and assumptions that accompany this software suite. In addition, validation of important cases, such as a shock tube test and

Riemann problem, are shown. Chapter 4 investigates the properties of the mass-fraction model where the results of the 1D mass-fraction model are compared to the results of higher-dimensional models. Lastly, Chapter 5 will discuss the conclusions reached in from the material in Chapter 4, and describe future uses for this model. The Appendix will provide additional details that were not developed in the main chapters.

Chapter 2

MATHEMATICAL MODEL

List of Symbols

Symbol	Description
ρ	Density [kg m^{-3}]
v	Velocity [m/s]
g	Acceleration due to gravity [m s^{-2}]
γ	Specific heat ratio
R	Specific gas constant
c_s	Speed of sound [m s^{-1}]
p	Pressure [Pa]
E	Energy [J]
q	Variables of state
H_s	Scale height [m]
H	Enthalpy [J]
k	Wave number [m^{-1}]
Y_s	Mass-Fraction density of species s
u	Velocity used for single gas model [m s^{-1}]
ω_A	Acoustic cutoff frequency
ω_N	Brunt-Väisälä frequency
χ'	Perturbation of variable " χ "
χ_r	Radial value of variable " χ "
χ_0	Background value of variable " χ "

2.1 Physical and Mathematical Basis

2.1.1 Stratified Atmosphere

Earth's middle atmosphere and lower thermosphere can be approximated as an ideal mixture of ideal gas comprising its major components O, O₂, and N₂. This approximation requires the atmosphere's highly variable components, e.g. water vapor or ozone, be treated separately from the primary atmospheric gases Salby [2012]. To begin, the equation of state for an ideal single-component gas takes the form:

$$p = \rho RT, \quad (2.1)$$

where p , ρ , and T refer to the pressure, density, and temperature of the gas, and $R = R^*/M$, where R is the specific gas constant, R^* is the universal gas constant, and M is the molecular mass of the gas. The equation of state and the hydrostatic equation can be applied to an unperturbed, isothermal atmosphere. Consider Newton's second law applied to an area dA ; the columns of air experience a force pdA and a column of air incrementally higher experiences a force $(p + dp)dA$. After the forces are balanced with buoyancy, the equilibrium equation that results is

$$\frac{dp}{dz} = -\rho g = -\frac{pg}{RT}. \quad (2.2)$$

In this relation, net vertical acceleration is zero and it is assumed that there are no other physical processes present. Equation 2.2 is known as the hydrostatic balance equation which describes a gas that is at rest White [2008]. It describes the vertical pressure gradient as a function of the gas layer's weight above it. The hydrostatic balance equation has an analytical solution under the assumption of a locally isothermal gas and a constant acceleration due to gravity. Equation 2.2, when integrated from a reference altitude z_0 to a higher altitude z , leads to a solution of an exponentially decaying density and pressure with altitude:

$$(p, \rho) = (p_0, \rho_0) \exp\left(-\int_{z_0}^z \frac{dz'}{H_s}\right), \quad (2.3)$$

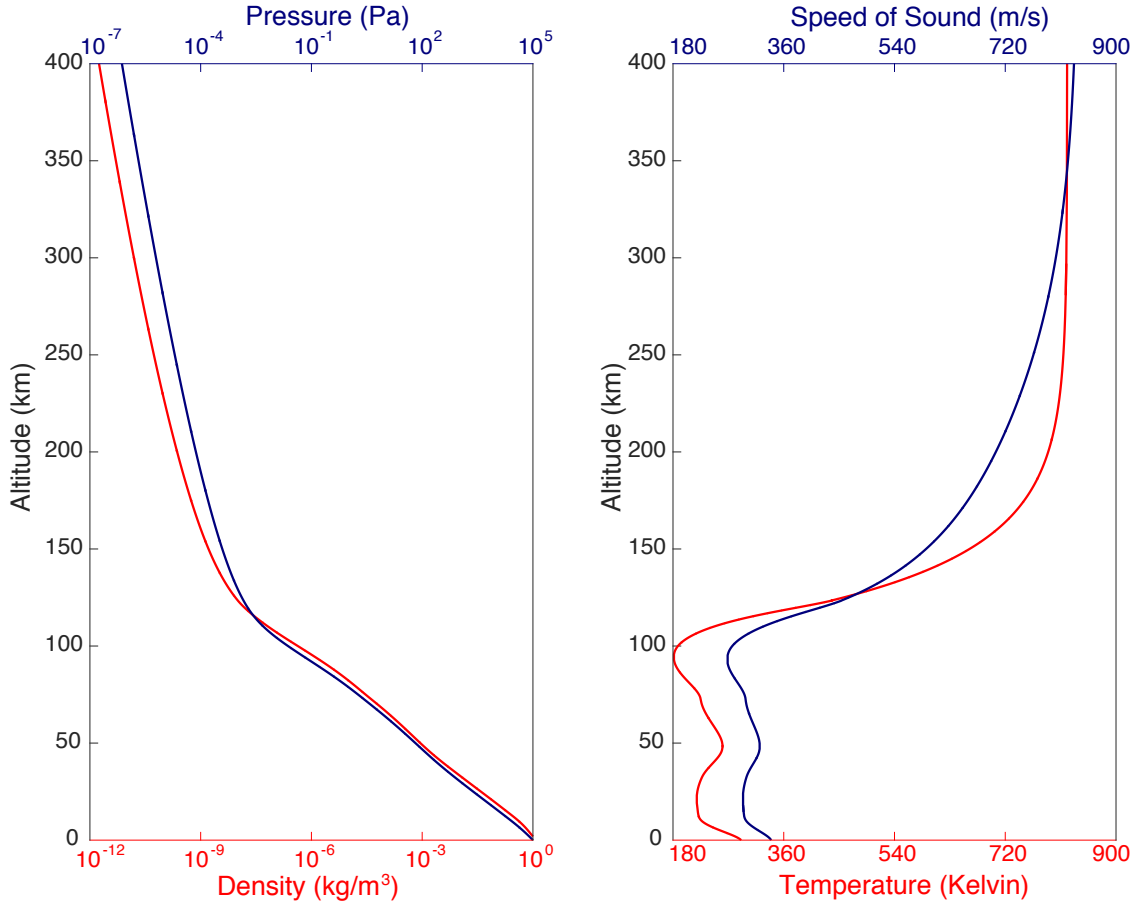


Figure 2.1: The atmosphere's density and pressure with altitude (left) and the temperature and speed of sound with altitude (right).

where the scale height H_s is introduced as $H_s = RT/g$. The scale height describes the altitude over which the atmosphere's density reduces by a factor of e (Euler's number). If the reference altitude $z_0 = 0$, the result of integration is

$$(p, \rho) = (p_0, \rho_0) \exp(-z/H_s). \quad (2.4)$$

The speed of sound is dependent on the compressibility of the medium through which it propagates, usually expressed as the material's Bulk Modulus.

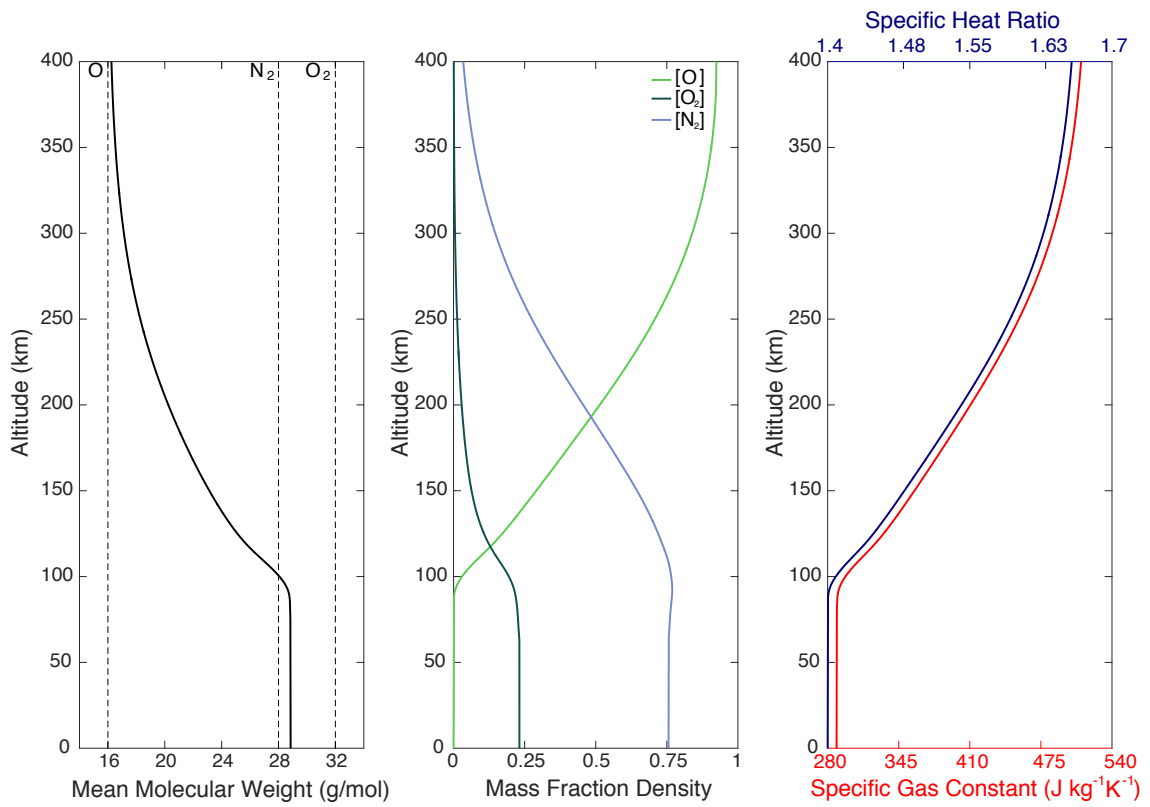


Figure 2.2: The mean molecular weight (left), mass fraction density (center), and the specific heat ratio and specific gas constant (right) as a function of altitude.

In the case of a gas, the compressibility depends on the specific heat ratio γ and pressure p , expressed as

$$c_s^2 = \gamma RT = \frac{\gamma p}{\rho}, \quad (2.5)$$

where $\gamma = c_p/c_v$ is the ratio of specific heat constant pressure c_p divided by specific heat constant volume c_v . The ratio of specific heat reflects the layers of the atmosphere that are mixed. The lower atmosphere is dominated by diatomic gases (N_2), where $\gamma = 1.4$, whereas in the upper atmosphere $\gamma = 1.67$, which is the value for monatomic gases. To calculate for the value in regions of mixed composition, the relation for specific heat ratio is given by Banks and Kockarts [1973]:

$$\gamma = \frac{7([\text{N}_2] + [\text{O}_2]) + 5[\text{O}]}{5([\text{N}_2] + [\text{O}_2]) + 3[\text{O}]}, \quad (2.6)$$

where the brackets $[\cdot]$ represent the number density of the compound inside the brackets. The definitions outlined above, in particular the locally isothermal atmosphere, are assumed to derive a linear dispersion relation for acoustic-gravity waves in Section 2.1.3.

2.1.2 Euler Equations

The Euler equations are a system of nonlinear partial differential equations that describe the conservation of momentum, mass, and energy in a compressible fluid:

$$\frac{\partial \rho}{\partial t} + \nabla \cdot (\rho \vec{v}) = 0, \quad (2.7)$$

$$\frac{\partial}{\partial t}(\rho \vec{v}) + \nabla \cdot (\rho \vec{v} \vec{v}) + \nabla p = -\rho \vec{g}, \quad (2.8)$$

$$\frac{\partial E}{\partial t} + \nabla \cdot \{(E + p)\vec{v}\} = -\rho \vec{g} \cdot \vec{v}. \quad (2.9)$$

They are closed under the ideal gas law and the definition of energy:

$$E = \frac{p}{\gamma - 1} + \frac{1}{2}\rho(\vec{v} \cdot \vec{v}). \quad (2.10)$$

These equations are a special case of the Navier-Stokes equations with no rotational, viscous, or thermal conduction terms. The Euler equations neglected terms, associated with the fluid's viscosity and thermal conduction, will be addressed together in the Section 2.1.4; rotational forces are negligible for waves considered in this thesis.

2.1.3 Linear Dispersion

To determine characteristics of a stratified atmosphere, the two dimensional linear Euler equations are considered for the conditions where a dispersion relation can arise. For this derivation, atmosphere with no background wind is assumed. In addition, density and pressure do not vary in the horizontal direction. The linearized state, in terms of atmospheric primitive variables, takes the following form:

$$\begin{pmatrix} \rho \\ p \end{pmatrix} = \begin{pmatrix} \rho_0 \\ p_0 \end{pmatrix} + \begin{pmatrix} \rho' \\ p' \end{pmatrix}, \quad \begin{pmatrix} v_x \\ v_z \end{pmatrix} = \begin{pmatrix} v_{\theta,x} \\ v_{\theta,z} \end{pmatrix} + \begin{pmatrix} v'_x \\ v'_z \end{pmatrix}$$

Where the subscript 0 represent the background values and the $'$ represent the perturbed value. If the background quantities remain time-invariant and the perturbations are assumed small enough to where the products of first order perturbations can be neglected, the two-dimensional, compressible, linearized Euler Equations for a compressible and stratified atmosphere are obtained:

$$\frac{\partial \rho'}{\partial t} = -\rho_0 \frac{\partial v'_x}{\partial x} - \rho_0 \frac{\partial v'_z}{\partial z} - v'_z \frac{\partial \rho_0}{\partial z}, \quad (2.11)$$

$$\frac{\partial v'_x}{\partial t} = -\frac{1}{\rho_0} \frac{\partial p'}{\partial x}, \quad (2.12)$$

$$\frac{\partial v'_z}{\partial t} = -\frac{1}{\rho_0} \frac{\partial p'}{\partial z} - \frac{\rho'}{\rho_0} g, \quad (2.13)$$

$$\frac{\partial p'}{\partial t} = -v'_z \frac{\partial p_0}{\partial z} - \gamma p_0 \left(\frac{\partial v'_x}{\partial x} + \frac{\partial v'_z}{\partial z} \right). \quad (2.14)$$

Equations 2.11-2.14 can be combined to determine a dispersion relation with the assumption that velocity and pressure are described with plane waves:

$$(v', p') = (v'_z, p'_z) \exp [j (k_x x - k_z z - \omega t)].$$

When the Euler equations and hydrostatic atmosphere assumptions are combined (see [Hines, 1960] for a complete derivation), a wave equation arises

$$\frac{d^2 v'_z}{dz^2} - \frac{g\gamma}{c_s^2} \frac{dv'_z}{dz} + \frac{k_x^2}{\omega^2} \left[\frac{g^2 \gamma}{c_s^2} - \omega^2 \right] v'_z = 0. \quad (2.15)$$

The perturbed gas vertical acceleration ($\partial v'_z / \partial z$) in Equation 2.15 is eliminated when the velocity is scaled by a factor of $\sqrt{\rho_s / \rho_0}$ where ρ_s is the density at a reference altitude. The scaled term is a result of the conservation of kinetic energy and the earlier assumption of hydrostatic equilibrium which has density exponentially decrease with altitude. The vertical velocity will also increase exponentially with altitude. The perturbed variables can be rescaled by:

$$v'_z = w'_z \sqrt{\frac{\rho_s}{\rho_0}}.$$

Using Equation 2.15, a wave equation for the normalized vertical wave perturbation is shown in Equation 2.16.

$$\frac{d^2 w'_z}{dz^2} + \left[\frac{\omega^2 - \omega_A^2}{c_s^2} - \frac{\omega^2 - \omega_N^2}{v_\phi^2} \right] w'_z = 0, \quad (2.16)$$

$$k_z^2 = \frac{\omega^2 - \omega_A^2}{c_s^2} - \frac{\omega^2 - \omega_N^2}{v_\phi^2}, \quad (2.17)$$

where $v_\phi = \omega / k_x$ is the horizontal phase velocity. The assumption of an isothermal stratified atmosphere helps to deduce intrinsic characteristics of the atmosphere that are relevant to this study. The Brunt-Väisälä frequency, ω_N , is the frequency at which a parcel of air in a stratified atmosphere, when displaced vertically, will naturally

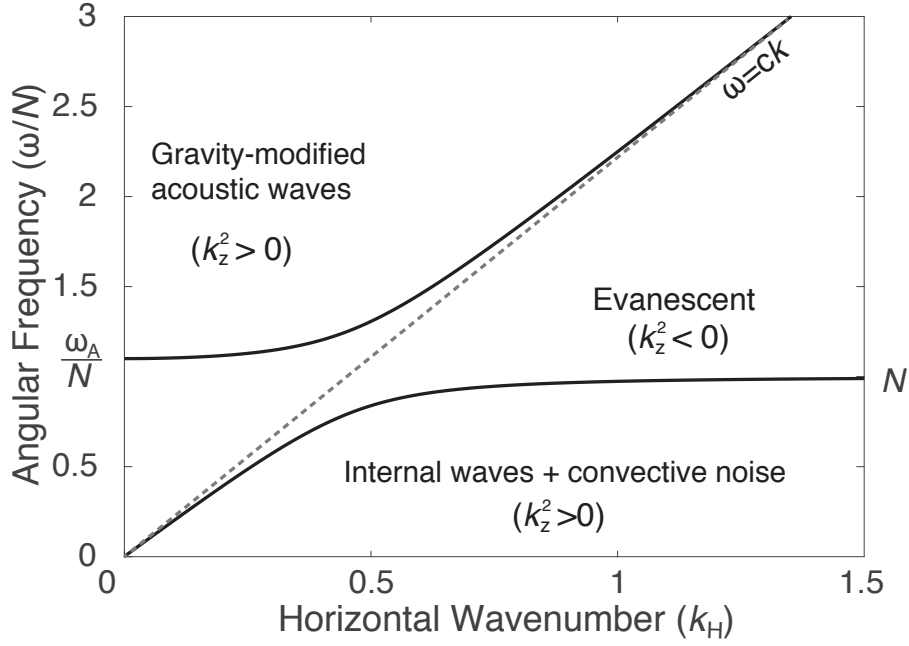


Figure 2.3: Dispersion curves for wave propagation in a compressible, gravitationally stratified medium for a given height in the atmosphere. Image adopted from Vigeesh et al. [2017] and Gossard and Hooke [1975].

oscillate. For this isothermal case it is:

$$\omega_N = \frac{g}{c_s} \sqrt{\gamma - 1}. \quad (2.18)$$

As this thesis focuses on acoustic waves, attention is also directed towards the acoustic cutoff frequency. The acoustic cutoff frequency, ω_A , is the minimum frequency of a vertically-propagating acoustic wave and can generally be defined by [Gossard and Hooke, 1975]

$$\omega_A^2 = \frac{1}{4} c_s^2 \left[\frac{d}{dz} \ln(\rho_0) \right]^2. \quad (2.19)$$

For acoustic wave motion in an isothermal atmosphere, as assumed in the derivation of Equation 2.16, the expression becomes:

$$\omega_A = \frac{g\gamma}{2c_s}. \quad (2.20)$$

These definitions help to characterize the types of problems that can be solved, by classifying wave propagation regimes.

2.1.4 Viscous Diffusion and Thermal Conduction

The Euler equations do not include viscous diffusion (molecular viscosity) or thermal conduction terms, which are important for acoustic wave dissipation in the thermosphere. As infrasonic acoustic waves propagate through the atmosphere, they experience damping by other processes as well, as described in the work done by Sutherland and Bass [2004]. However, these terms are neglected due to the spectra of interest. The primary diffusion processes take the form of Fick's second Law, within the one-dimensional form as follows

$$\frac{\partial \Phi}{\partial t} = \mathcal{D} \frac{\partial^2 \Phi}{\partial x^2}, \quad (2.21)$$

where Φ is the quantity being diffused and \mathcal{D} is the diffusion coefficient. The expressions for viscous and thermal diffusion can be deduced after the Navier-Stokes equation are simplified from the Euler equations; to arrive at an expression in the same form as Equation 2.21 that numerically can be solved by time-splitting. The Navier-Stokes momentum equation is realized when viscosity is added to the Euler equations.

$$\frac{\partial(\rho \vec{v})}{\partial t} + \nabla(\rho \vec{v} \vec{v}) + \nabla p = \mu \nabla^2 \vec{v} + \frac{1}{3} \nabla(\mu \nabla \cdot \vec{v}) - \rho \vec{g}, \quad (2.22)$$

The Euler equations and diffusive terms are solved separately using a time-split method which takes the following form

$$\frac{\partial u}{\partial t} = F(u) + G(u), \quad (2.23)$$

where $F(u), G(u)$ represent parts of a differential equation that will be solved separately. The general Euler equations prior to have been established in Equation 2.7-2.9 prior to, and the 1D numerical discretization will be presented in Chapter 3. The following address the diffusive equations:

Thermal Conduction

Thermal conductivity for this study is considered for the perturbed states in the Euler equations. An expression modeling the effects of thermal conduction can be derived starting from the conservation of energy for a fluid in the atmosphere. In simplest form, thermal conduction is expressed via Fourier's Equation

$$\vec{q} = -\kappa \nabla T, \quad (2.24)$$

where κ is the thermal conductivity coefficient. The expression for heat flux combined with the equations given in the diffusion section (another form of the Navier-Stokes equations) results in Equation 2.25

$$\frac{\partial E}{\partial t} = \underbrace{-\nabla \cdot \{(E + p)\vec{v}\} - \rho \vec{g} \vec{v}}_{\text{Euler energy equation}} + \underbrace{(\nabla \cdot \tau) \cdot \vec{v} + \nabla \cdot \vec{q}}_{\text{viscous and thermal conduction}}, \quad (2.25)$$

where τ are the stress tensor in $[\text{N}/\text{m}^2]$. The notation here indicates two portions of the conservation equation that will be solved using a time-split method. The focus of this section is on the viscous and thermal conductivity portion which take the form

$$\frac{\partial E^*}{\partial t} = \nabla \cdot \vec{q} + (\nabla \cdot \tau) \cdot \vec{v}, \quad (2.26)$$

where E^* represents the time-split energy that solves the thermal conduction separately from the Euler energy equation in Equation 2.25. The effects of viscous stress on energy redistribution is negligible compared to the thermal conduction, so the viscous tensor term is approximated using the form shown by recalculating the kinetic energy distributed by viscosity. If the energy in Equation 2.26 is defined as

$$E^* = q = \rho c_p T, \quad (2.27)$$

where c_p is the specific heat, constant pressure. With the assumptions listed above, the one dimensional thermal conduction equation:

$$\frac{\partial T^*}{\partial t} = \frac{\kappa}{\rho c_p} \frac{\partial^2 T^*}{\partial z^2} = \alpha \frac{\partial^2 T^*}{\partial z^2}, \quad (2.28)$$

where T^* is the time-split Euler temperature, and α is the thermal diffusivity in m^2s^{-1} . Equation 2.28 takes the form of the one dimensional heat equation, which has well established numerical solutions that are presented in Section 3. Thermal diffusivity is dependent on chemical composition, density, temperature, etc. and are usually approximated since there isn't a useful general solution. The thermal conductivity coefficients κ used in this thesis are determined with an empirical relationship as shown in Rees [1989]

$$\kappa = \frac{\sum_j C_j n_j}{\sum_j n_j} T^B. \quad (2.29)$$

The parameter B is a fit coefficient and has a value of $B = 0.69$ for all major atmosphere species. n_j is the concentration of the j th constituent, C_j is the numerical coefficients approximated for the empirical equations (whose values are shown in Table 2.1), κ is the thermal conductivity in $[\text{erg cm}^{-1}\text{s}^{-1}\text{K}^{-1}]$. An example of a thermal diffusivity profile (m^2/s) that was used in this thesis is shown in Figure 2.4.

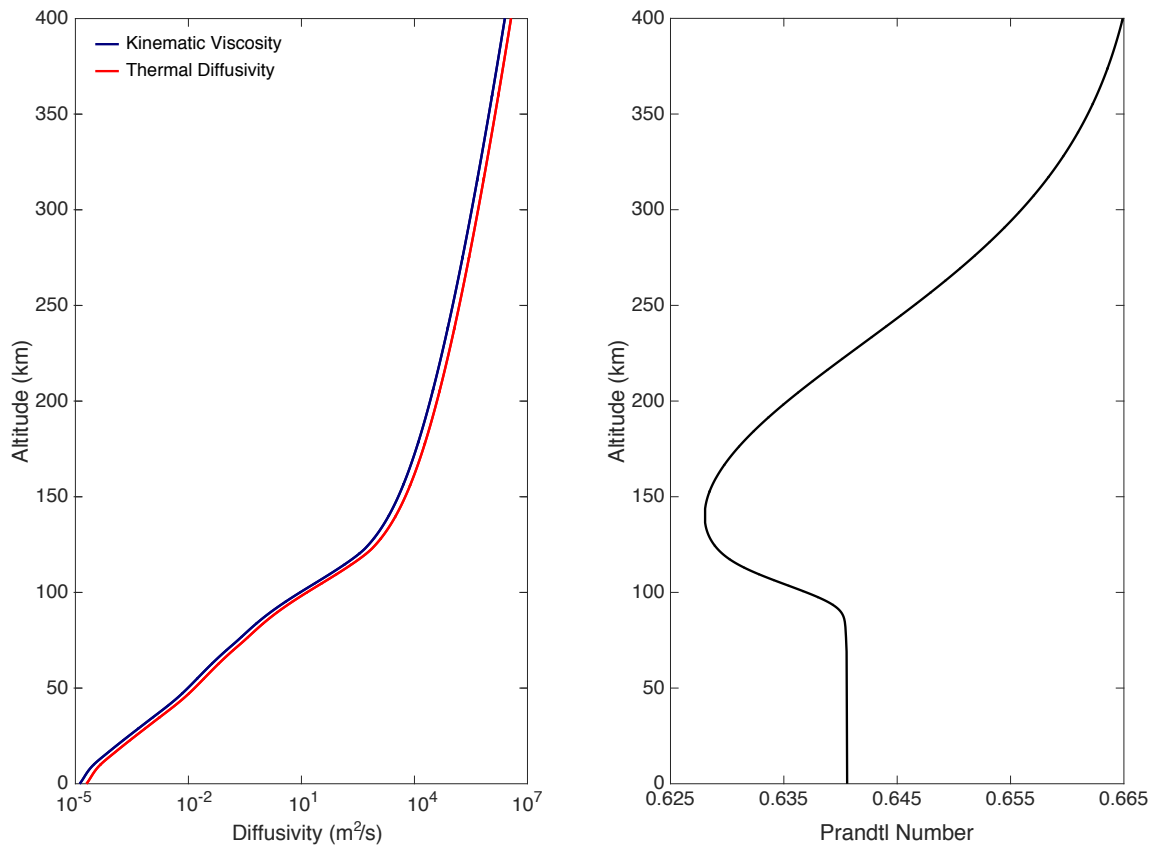


Figure 2.4: The empirical dynamic viscosity and thermal conductivity derived in Rees [1989] with altitude (left). The Prandtl number (right) is defined as the ratio of thermal diffusivity to kinematic viscosity.

Table 2.1: Tables of the major atmospheric constituents and their fit parameters for thermal conductivity and viscosity obtained from Rees [1989]

j	A_j	C_j
N ₂	3.43×10^{-6}	56
O ₂	4.03×10^{-6}	56
O	3.90×10^{-6}	75.9
He	3.84×10^{-6}	299
H	1.22×10^{-6}	379

Viscosity

Viscosity describes a fluid's resistance to deformation, and measures how strongly layers are coupled by friction. Molecular viscosity becomes significant in the atmosphere due to large collisional scales. These processes become significant in the upper atmosphere, for example dynamic viscosity, μ in [Pa · s], is used as the constant of proportionality in Newton's Law to relate shear stress to a velocity gradient and kinematic viscosity, $\nu = \mu/\rho$ in m²s⁻¹ will be used in the final numerical expression for applied physical viscosity. The momentum equation from Equation 2.22 divided by the density (with the assumption that the perturbed density is negligible is separated into a time-split format. Considering only the viscous terms:

$$\frac{\partial \vec{v}^*}{\partial t} = \nu \nabla^2 \vec{v} + \frac{\nu}{3} \nabla(\nabla \cdot \vec{v}) \quad , \quad (2.30)$$

where the kinematic viscosity, $\nu = \mu/\rho$ has replaced the dynamic viscosity. The two labeled portions of Equation 2.30 indicate the viscous effects will take a similar form to the thermal conduction solution. In one-dimension, the viscous equation takes the form

$$\frac{\partial v_z^*}{\partial t} = \frac{4\nu}{3} \frac{\partial^2 v_z^*}{\partial z^2} \quad , \quad (2.31)$$

where v_z^* is the time split vertical velocity that is solved separately from the Euler Equations. Similar to the thermal diffusivity calculation, kinematic viscosity depends on several parameters. To calculate the kinematic viscosity, an empirical expression

derived by Rees [1989] is used to calculate the dynamic viscosity η_j

$$\eta = \sum_j A_j T^B, \quad (2.32)$$

where η_j is the dynamic viscosity in $[\text{gm cm}^{-1}\text{s}^{-1}]$, and A_j is the numerical coefficients approximated for the empirical equations (shown in Table 2.1). A typical profile for the molecular viscosity with altitude is shown in Figure 2.4. Molecular Theory states conductivity κ is directly proportional to ν . For air in a temperature range of $200\text{K} \leq T \leq 1000\text{K}$ with a constant specific heat at constant pressure c_p [Rees, 1989]

$$Pr \equiv \frac{\nu \rho c_p}{\kappa} \approx \frac{4\gamma}{9\gamma - 5}, \quad (2.33)$$

where Pr is the Prandtl number which is a metric to compare momentum diffusion to thermal diffusion. Prandtl values less than one indicate thermal diffusion is the dominate process in the fluid. Eddy viscosity which results from small-scale vorticity is ignored since its effects are unimportant in the thermosphere where molecular viscosity is dominant.

2.1.5 Chapter Summary

This chapter has presented the mathematical basis and the acoustic wave equations of motion and dispersion used in this thesis. It also provided a reference for the numerical methods presented in the next section. Parameters that characterize a one-gas system and a stratified atmosphere, such as the ideal gas law for a mixture, the speed of sound, and molecular diffusion and thermal conductivities were defined. The Euler equations, a simplified, non-diffusive Navier-Stokes equations, were presented in their one-dimensional form. Diffusive processes, molecular viscosity and thermal conduction, are important when discussing the processes that occur in the thermosphere, will be time-split from the Navier-Stokes equations and approximated in one-dimension in the form of Fick's Law.

Chapter 3

NUMERICAL MODEL IMPLEMENTATION

This chapter focuses on the numerical methods that are used to solve the one-dimensional Navier-Stokes equations. The methods discussed apply Leveque's Conservation Laws Package, or CLAWPACK [LeVeque, 2002] to solve the Euler equations. Using a Flux-limited second order Godonuv method with an approximate Riemann solver. The diffusive parts of the Navier-Stokes equation are time-split and solved with a forward in time, centered in space (FTCS) explicit Euler method. Compositional variation via an advected mass-fraction density is introduced and extended into higher-dimensional cases under the assumption of radial symmetry. The mass-fraction model ability to handle discontinuities is validated with a shock tube test as done in Sod [1978].

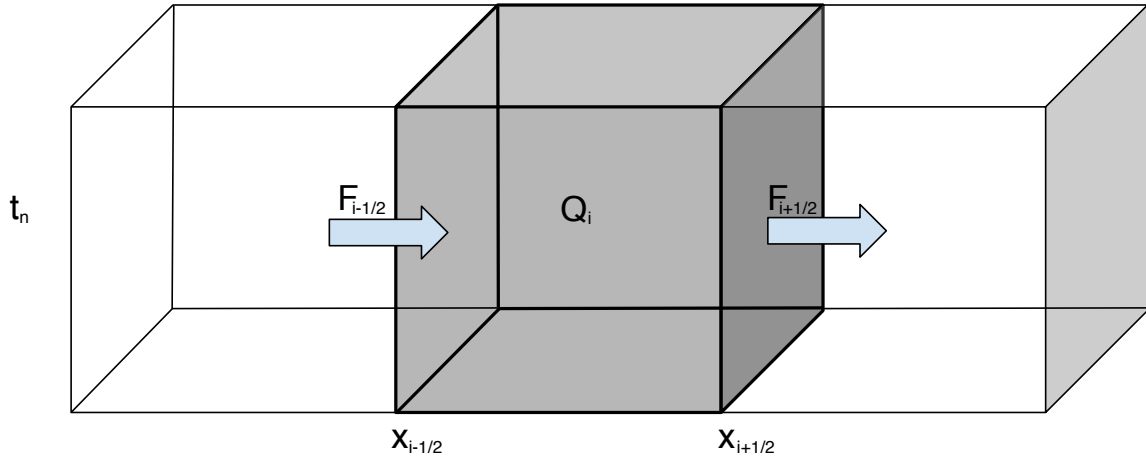


Figure 3.1: A grid perspective of a finite volume cell with a left and right flux going into (and out of) it.

3.1 Finite Volume Methods

The Euler equations are a hyperbolic system of conservation laws that, in one-dimension, take the following form:

$$\frac{\partial q}{\partial t} + \frac{\partial f(q)}{\partial x} = \Psi, \quad (3.1)$$

where Ψ is a source term and $f(q)$ is the flux function of q , which is the conserved quantity. A numerical approach involves dividing space and time into a grid, or cell, similar to that seen in Figure 3.1. After the quantities in (Equation 3.1) are integrated for a cell the general form of an FVM arises

$$Q_i^{n+1} = Q_i^n - \frac{\Delta t}{\Delta x} (F_{i+1/2}^n - F_{i-1/2}^n), \quad (3.2)$$

where Q_i^n approximates the average value over the i th cell at time t_n , and $F_{i\pm 1/2}^n$ are the fluxes based on the approximate values of Q . Note: The subscript i refers to a spatial grid, whereas superscripts n refer to the temporal grid. There are myriad FVM variations that exist, which may be appropriate for different types of problems. The reader is encouraged to read LeVeque [2002] to learn more about FVMs.

Stability of FVMs are described using the Courant-Friedrich Lewy (CFL) number, which imposes the condition: "*A numerical method can be convergent only if its numerical domain of dependence contains the true domain of dependence of the PDE, at least in the limit as Δt and Δx to zero*" [LeVeque, 2002]. For the case of the Euler equations information cannot travel faster than the local speed of sound, and for our method, it should not move further than one cell per time step. The CFL condition is quantified by

$$\text{CFL} \equiv \left| \frac{u\Delta t}{\Delta x} \right| \leq 1, \quad (3.3)$$

where u is the speed at which information propagates in the medium, Δx , Δt are the grid size in space and time respectively. A notable stability complication can occur when the problem involves discontinuities, which is especially important due to Earth's stratified atmosphere, and the nature of processes such as shocks that can occur in the atmosphere. The FVM used by CLAWPACK is a second order Godunov Method [LeVeque, 2002], which solves the Riemann Problem at each boundary. Thus, it adapts naturally to problems with steep solutions or shocks.

3.1.1 Godunov's Wave-Propagation Method

Godunov's method is ideal for nonlinear acoustic waves and shocks because it solves the Riemann problem at each boundary and, although it is alone first order accurate, it can be reconstructed to achieve higher resolution. The method used is a flux limited wave propagation method that takes a similar form to (Equation 3.2). Consider the quasi-linear form of a system of conservation equations:

$$\frac{\partial \vec{q}}{\partial t} + \mathbf{A} \frac{\partial \vec{q}}{\partial x} = 0, \quad \mathbf{A} = \frac{\partial f(\vec{q})}{\partial \vec{q}}, \quad (3.4)$$

where \mathbf{A} is the Jacobian matrix which will define the characteristics of the system of equations.

F-wave Method From Bale et al. [2003]

For a linear system, the solution to the Riemann problem can be expressed as a set of waves. The Jacobian matrix \mathbf{A} can be characterized with eigenvalues λ and eigenvectors R if \mathbf{A} is defined as $\mathbf{A} = R\Lambda R^{-1}$ where:

$$\Lambda^\pm = \begin{bmatrix} (\lambda^1)^\pm & & & \\ & (\lambda^2)^\pm & & \\ & & \ddots & \\ & & & (\lambda^m)^\pm \end{bmatrix} \quad (3.5)$$

$$Q_i - Q_{i-1} = \sum_{p=1}^m \alpha_{i-1/2}^p r^p \equiv \sum_{p=1}^m \mathcal{W}_{i-1/2}^p$$

The characteristic variables \mathcal{W} can be viewed as "waves" defined as $\mathcal{W} = R^{-1}q$. They are referred to as waves since the state variable Q is seen as a superposition of eigenvectors in space-time, or equivalently a superposition of waves with eigenvalues λ^m . To put the original FVM in terms of "waves" transforms Equation 3.2 to:

$$Q_i^{n+1} = Q_i^n - \frac{\Delta t}{\Delta x} (A^+ \Delta Q_{i-1/2} + A^- \Delta Q_{i+1/2}) \quad (3.6)$$

$$F_{i\pm 1/2}^n = A^\pm \Delta Q_{i\pm 1/2}$$

where the superscripts \pm refers to the values derived from right (+) or left (-) going waves. For the Euler equations, the Roe solver from Roe [1981] is used to define the Jacobian matrix \mathbf{A} .

This thesis uses the flux-based wave decomposition, or "f-wave" method, created by Bale et al. [2003] that decomposes the *flux difference* as a linear combination of

eigenvectors R . The solution for Q_i^{n+1} is given by:

$$Q_i^{n+1} = Q_i^n - \underbrace{\frac{\Delta t}{\Delta x} (A^+ \Delta Q_{i-1/2} + A^- \Delta Q_{i+1/2})}_{\text{Godunov Method}} - \underbrace{\frac{\Delta t}{\Delta x} (\tilde{F}_{i+1/2} - \tilde{F}_{i-1/2})}_{\text{Flux-Limited Waves}} \quad (3.7)$$

$$\tilde{F}_{i-1/2} = \frac{1}{2} \sum_{p=1}^{M_w} \text{sgn}(s_{i-1/2}^p) \left(1 - \frac{\Delta t}{\Delta x} |s_{i-1/2}^p| \right) \tilde{Z}_{i-1/2}^p.$$

where s refers to the speed of sound of the wave that arises from the eigenvalues and $\tilde{Z}_{i-1/2}^p$ refers to the flux limited "f-wave". The "f-wave" and "wave" methods take similar forms in terms of the characteristics. The eigenvalues in Equation 3.5 do not change with the "f-wave" method, but the "f-wave" definition is based on flux differencing:

$$f_i(Q_i) - f_{i-1}(Q_{i-1}) - \Delta x \Psi_{i-1/2} = \sum_{p=1}^m \beta_{i-1/2} r_{i-1/2}^p \equiv \sum_{p=1}^m \mathcal{Z}_{i-1/2}^p \quad (3.8)$$

$$\beta_{i-1/2} = R_{i-1/2}^{-1} (f_i(Q_i) - f_{i-1}(Q_{i-1}) - \Delta x \Psi_{i-1/2}).$$

Numerical solutions to partial differential equations are susceptible to numerical diffusion, dispersion, artificial oscillations, and smoothing of wave fronts, especially in fluid dynamics. To account for these processes, flux limiters have been developed to sustain realistic values and eliminate artifacts with controlled numerical viscosity. Limiters $\phi(\theta)$ depends on the slope θ of the state variable and the sign of the velocity:

$$\theta_{i-1/2}^p = \frac{\mathcal{Z}_{I-1/2}^p}{\mathcal{Z}_{i-1/2}^p}, \quad I = \begin{cases} i-1 & \text{if } \bar{u} > 0 \\ i+1 & \text{if } \bar{u} < 0 \end{cases} \quad (3.9)$$

The limiter used in CLAWPACK is the monotonized central limiter developed by van Leer [1974], given by:

$$\phi(\theta) = \max [0, \min (2\theta, 0.5(1 + \theta), 2)], \quad (3.10)$$

which tends towards $\phi = 2$ as $\theta \rightarrow \infty$. Limiter functions can also be used to raise

the order of accuracy of another method. Godunov's method is first order accurate, but with a Flux limiter that satisfies the second order criteria of Total Variation Diminishing (TVD), the method approaches second order accuracy. The reader is encouraged to read Sweby [1984] to learn about several of the flux limiter types and TVD criteria. CLAWPACK applies limiters to "waves" instead:

$$\widetilde{\mathcal{W}}_{i-1/2}^p = \phi(\theta_{i-1/2}^p) \mathcal{W}_{i-1/2}^p, \quad (3.11)$$

$$\widetilde{\mathcal{Z}}_{i-1/2}^p = s_{i-1/2}^p \widetilde{\mathcal{W}}_{i-1/2}^p = \phi(\theta_{i-1/2}^p) \mathcal{Z}_{i-1/2}^p. \quad (3.12)$$

The CFL condition still abides by the definition in Equation 3.3 to ensure stability.

The above discretizes the Euler equations which includes gravity. The value for gravity has to balance the model in steady state, so from the relation for hydrostatic equilibrium (Equation 2.2), a discretized expression for the acceleration due to gravity arises:

$$g_i = -\frac{p_i^* - p_{i-1}^*}{\Delta z} \frac{2}{\rho_i^* + \rho_{i-1}^*}, \quad (3.13)$$

where the subscript asterisks are used to denote the initial state. The reason for the approximation can be seen visually in Figure 3.2. The value of gravity experiences some fluctuations away from average especially in the lower thermosphere. Since the empirical atmosphere does not exhibit an ideal steady state, the value of gravity derived from the hydrostatic equilibrium fits the uses of this model better than the Newtonian approximation, balancing the atmosphere to high precision.

3.1.2 Methods for Parabolic Equations

The diffusion equations are solved via a time-split method which follows the Euler Equations (as shown in the previous sections) and accounts for the effects of thermal conductivity and viscosity. The diffusion equations that are considered in this thesis both have a similar form of one-dimensional Fick's Law as described in Chapter 2. Similar to the Euler equations, the diffusive equations can be discretized into a grid (Figure 3.3, right panel). A solution to a discrete one-dimensional parabolic

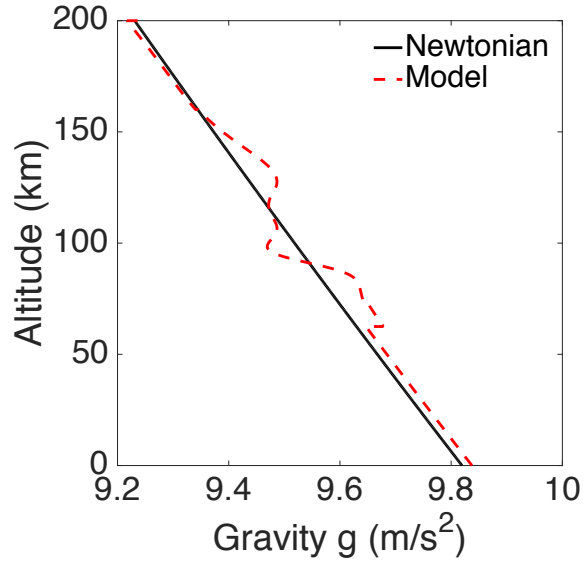


Figure 3.2: Gravity as calculated by Newton’s law (black) and calculated using NRLMSISE-00 atmospheric properties with hydrostatic equilibrium.

equation takes the form of a Finite Difference Method (FDM). Common FDMs include forward-in-time-centered-in-space (FTCS), backward-in-time-centered in space (BTCS), Crank-Nicholson, etc. The two FDMs discussed in this thesis are the implicit Euler (FTCS) and the explicit Euler (BTCS). Both methods are second-order-in-space/first-order-in-time and can take the form of

$$U_i^{n+1} = \mathcal{A}U_i^n \quad 1 \leq i \leq n - 1, \quad (3.14)$$

where \mathcal{A} is used to denote the symmetric, constant coefficient matrix that are involved with FDM problems. In methods similar to FTCS, the constant coefficient matrix is a diagonal dominant tridiagonal matrix. The properties of the \mathcal{A} shape the solution, and can be used to determine an efficient way to solve the system. FDMs have stability restrictions which can be described with the Fourier Number (Fo), but further discussions are simplified if the matrix properties of the \mathcal{A} matrix is used to characterize a method’s stability.

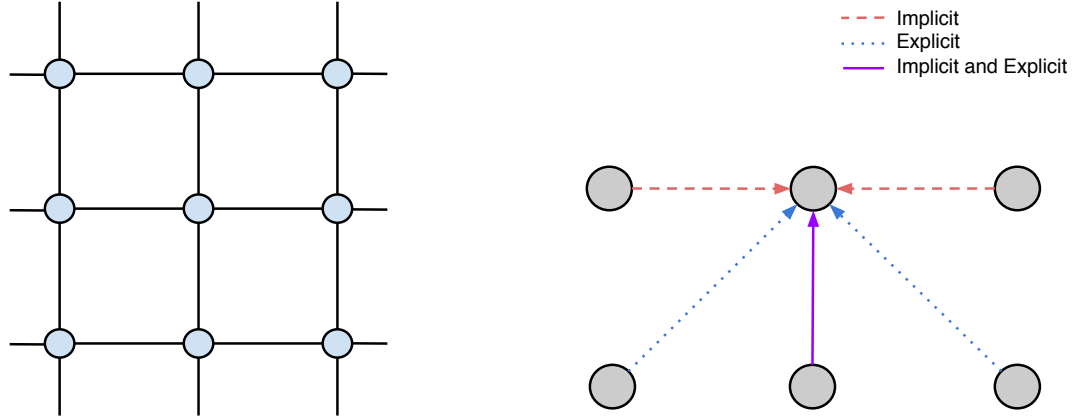


Figure 3.3: A grid used in a one dimensional finite difference method (left) and the progression of the discretized diffusion values (right).

Implicit FDM

The implicit FDM is a method that requires more calculations per time step than explicit methods, but guarantees convergence. This method takes the form

$$u_j^{n+1} = u_j^n + \frac{\mathcal{D}\Delta t}{\Delta z^2}(u_{j+1}^{n+1} - 2u_j^{n+1} + u_{j-1}^{n+1}), \quad (3.15)$$

$$\mathcal{A}_I U_i^{n+1} = U_i^n. \quad (3.16)$$

where \mathcal{A}_I refers to the implicit \mathcal{A} matrix from Equation 3.14. The matrix \mathcal{A}_I has the form of a tridiagonal matrix

$$\mathcal{A}_I = \begin{bmatrix} 1 + 2r & -r & & & \\ -r & 1 + 2r & -r & & \\ & \ddots & \ddots & \ddots & \\ & & -r & 1 + 2r & -r \\ & & & -r & 1 + 2r \end{bmatrix}, \quad (3.17)$$

where $r = \mathcal{D}\Delta t(\Delta z^2)^{-1}$. This method is unconditionally stable which makes it susceptible to converging to an approximate solution. The implicit method is preferred for problems where the diffusion requires a larger time step. However, the explicit solution will be used for this thesis.

Explicit FDM

Arguably the most well known method is the explicit forward in time, centered in space method which has a similar form to the implicit FDM, but with all known variables on the right-hand-side. This takes the form, [Potter et al., 1976]

$$u_j^{n+1} = u_j^n + \frac{\mathcal{D}\Delta t}{\Delta z^2}(u_{j+1}^n - 2u_j^n + u_{j-1}^n), \quad (3.18)$$

$$U_i^{n+1} = \mathcal{A}_E U_i^n. \quad (3.19)$$

or, in matrix form:

$$\mathcal{A}_E = \begin{bmatrix} 1 - 2r & r & & & & & \\ & r & 1 - 2r & r & & & \\ & & \ddots & \ddots & \ddots & & \\ & & & r & 1 - 2r & r & \\ & & & & r & 1 - 2r & \end{bmatrix}, \quad (3.20)$$

where \mathcal{A}_E refers to the \mathcal{A} matrix for the explicit method, and r has the same definition that is shown for the implicit method. Unlike the implicit BTCS, this method is conditionally stable and is constrained by

$$\text{Fo} = \frac{\mathcal{D}\Delta t}{\Delta z^2} \leq \frac{1}{2}, \quad (3.21)$$

where Fo is the numerical Fourier number. If the condition above is met, this method is favorable since it requires less calculations per time step and is easier to implement. The implicit method requires more computational calculation time and its unconditional stability also makes it susceptible to inaccuracy for long time steps. The accuracy of the explicit solution is beneficial and it can be applied at a low cost.

3.1.3 Mass-Fraction Density

This thesis explores numerical solutions to the one-dimensional Euler equations with the addition of an advected mass fraction density to describe modulation of composition. This model treats the atmosphere as a multi-constituent single gas that moves with velocity u , under the influence of gravity and diffusion. The ideal gas law and the Euler equations assume a single fluid that moves with a uniform velocity, appropriate for a multi-constituent gas where the species are coupled. Alternative methods would also require equations of motion, internal energy, and state for each of the species and the effects due to collisions, similar to Hickey et al. [2015]. Instead, compositional variation is realized through the mass fraction density, as proposed by Hickey et al. [2001] in a single fluid. Equations 2.7 - 2.9 are shown in one dimension:

$$\begin{pmatrix} \rho \\ \rho u \\ E \end{pmatrix}_t + \begin{pmatrix} \rho u \\ \rho u^2 + p \\ u(E + p) \end{pmatrix}_x = \begin{pmatrix} 0 \\ -\rho g \\ -\rho g u \end{pmatrix}, \quad (3.22)$$

$$E = \frac{p}{\gamma - 1} + \frac{1}{2}\rho u^2. \quad (3.23)$$

The latter is an updated equation of state and the subscripts represent partial derivatives $(\cdot)_t, (\cdot)_x$ denotes time and spatial derivative respectively. It is convenient to work in terms of its quasilinear form. Equation 3.4 applied to the Euler equations become

$$\mathbf{A} = \begin{pmatrix} 0 & 1 & 0 \\ \frac{1}{2}(\gamma - 3)u^2 & (3 - \gamma)u & \gamma - 1 \\ \frac{1}{2}(\gamma - 1)u^3 - uH & H - (\gamma - 1)u^2 & \gamma u \end{pmatrix}, \quad (3.24)$$

$$\vec{q} = [\rho, \rho u, E]^T,$$

Enthalpy is introduced as $H = \rho(E + p)^{-1}$. The addition of mass-fraction density expands the Jacobian matrix shown in Equation 3.24 but preserves the original three. The changes will be explored in the following sections. The mass fraction density of a species "s", Y_s , is defined as the ratio of the species substance to the total substance

[Abgrall and Karni, 2000].

$$Y_s = \frac{\rho_s}{\rho}.$$

An important trait about the mass fraction density is $Y_s \in [0, 1]$. This becomes important in determining the validity of the mass fraction density solution. A non-conservative mass fraction density and a conservative mass fraction density were investigated in this thesis. The latter leads to different forms of additional advection equations. Note that in the cases shown γ , ν , α , and R are functions of composition (tracked by the mass fraction) and thus updated continuously throughout the simulations.

Non-conservative Mass Fraction Density

The non-conservative mass fraction density takes the form of a linear advection equation. In one dimension:

$$\frac{\partial Y_s}{\partial t} + u \frac{\partial Y_s}{\partial x} = 0, \quad (3.25)$$

where Y_s denotes the mass fraction density of species "s". The addition of one species results in a simple change to the Jacobian matrix

$$\mathbf{A} = \begin{pmatrix} 0 & 1 & 0 & 0 \\ \frac{1}{2}(\gamma - 3)u^2 & (3 - \gamma)u & \gamma - 1 & 0 \\ \frac{1}{2}(\gamma - 1)u^3 - uH & H - (\gamma - 1)u^2 & \gamma u & 0 \\ 0 & 0 & 0 & u \end{pmatrix}, \quad (3.26)$$

$$\vec{q} = [\rho, \rho u, E, Y_1]^T. \quad (3.27)$$

The addition of n_s species results in:

$$\mathbf{A} = \begin{pmatrix} 0 & 1 & 0 & 0 & \cdots & 0 & 0 \\ \frac{1}{2}(\gamma - 3)u^2 & (3 - \gamma)u & \gamma - 1 & 0 & 0 & \cdots & 0 \\ \frac{1}{2}(\gamma - 1)u^3 - uH & H - (\gamma - 1)u^2 & \gamma u & 0 & 0 & \ddots & \vdots \\ 0 & 0 & 0 & u & \ddots & \ddots & \vdots \\ 0 & \cdots & \ddots & \ddots & \ddots & & \vdots \\ \vdots & & & & & \ddots & 0 \\ 0 & 0 & 0 & 0 & 0 & 0 & u \end{pmatrix}, \quad (3.28)$$

$$\vec{q} = [\rho, \rho u, E, Y_1, \cdots, Y_{n_s-1}]^T \quad n_s \geq 1, \quad (3.29)$$

where n_s is the number of species. The mass fraction density of the remaining gas Y_{n_s} can be determined from

$$Y_{n_s} = 1 - \sum_{i=1}^{n_s-1} Y_i. \quad (3.30)$$

The f-waves used in the Euler equations are unaffected by the extra terms of u since this version is non-conservative. If \mathcal{W} from Equation 3.5 is defined as $\mathcal{W} = R^{-1}\alpha$, the non-conservative mass-fraction density method would define as $\alpha = Y_{1,L} - Y_{1,R}$.

Conservative Mass-Fraction Density

The conservative mass-fraction density advects the quantity ρY_s

$$\frac{\partial(\rho Y_s)}{\partial t} + \frac{\partial(\rho u Y_s)}{\partial x} = 0. \quad (3.31)$$

The Jacobian matrix that follows for n_s species is:

$$\mathbf{A} = \begin{pmatrix} 0 & 1 & 0 & 0 & \cdots & \cdots & 0 \\ \frac{1}{2}(\gamma - 3)u^2 & (3 - \gamma)u & \gamma - 1 & 0 & 0 & \cdots & 0 \\ \frac{1}{2}(\gamma - 1)u^3 - uH & H - (\gamma - 1)u^2 & \gamma u & 0 & 0 & \ddots & \vdots \\ -uY_1 & Y_1 & 0 & u & \ddots & \ddots & \vdots \\ -uY_2 & Y_2 & 0 & 0 & \ddots & & \vdots \\ \vdots & \vdots & \vdots & \vdots & \ddots & \ddots & 0 \\ -uY_{n-1} & Y_{n-1} & 0 & 0 & \cdots & 0 & u \end{pmatrix}, \quad (3.32)$$

$$\vec{q} = [\rho, \rho u, E, \rho Y_1, \dots, \rho Y_{n-1}]^T \quad n_s \geq 1. \quad (3.33)$$

The last species can be determined from Equation Equation 3.30. The validation and derivation of the conservative mass-fraction density is in Appendix A. Mass-fraction density is a conservative quantity, so the use of a conservative advection equation seems natural. However, the characteristic equations that arise from the conservative mass-fraction density add complexity to the solution of the systems of equations since the f-waves are scaled by the mass-fraction density. The impact of the conservative versus the non-conservative mass fraction density on species evolution in time for infrasonic waves were found to produce negligible effects such that the non-conservative version is used in this thesis.

3.1.4 Multi-dimensional Symmetry

Scenarios that involve radial symmetry can often be transformed from a complex multi-dimensional problem to a one-dimensional problem. If the Euler equations can be solved along a single coordinate variable r , often with a geometric source term,

such that terms that solely depend on the θ -direction can be ignored [LeVeque, 2002]:

$$\begin{aligned}\rho_t + (\rho U)_r &= -\frac{\alpha}{r}(\rho U), \\ (\rho U)_t + (\rho U^2 + p)_r &= -\frac{\alpha}{r}(\rho U^2), \\ E_t + ((E + p)U)_r &= -\frac{\alpha}{r}((E + p)U).\end{aligned}\tag{3.34}$$

Here $\alpha = n_{\text{dim}} - 1$, where α is the geometric coefficient, n_{dim} is the number of dimensions; $n_{\text{dim}} = 1, 2, 3$ for cartesian, cylindrical, and spherical symmetry respectively. Radially symmetric solutions are useful in testing and validation of numerical codes. There are often geometric sources of acoustic waves that are known to have radial symmetry; several examples are shown Chapter 4.

3.1.5 Riemann Solver Validation

The Sod problem, outlined by Sod [1978], is a one-dimensional discontinuity problem that can reveal a numerical scheme's ability to capture shocks and contact discontinuities with a small number of cells. The Sod problem initial state and properties of the final state are shown in Figure 3.4. A shock tube, closed at its ends and divided into two equal regions by a thin diaphragm, is filled with the same gas, but with different thermodynamic properties, namely pressure and density, at rest. Once the diaphragm is ruptured, a high-speed flow is initiated, which propagates from the region with more energy to the region with less energy. The gas at high pressure expands through rarefaction waves and flows into the low pressure. As a result, the low-pressure region is compressed, so much that a shock wave is generated. The initial separation of the gases is maintained through a fictitious discontinuous membrane that travels towards the lower pressure gas. The Riemann problem is established by the discontinuous physical properties that occur across the shock wave and contact discontinuity. For the shock, there is only a jump discontinuity in the density. The Sod test can be applied to the Euler equations under the assumption of an isothermal system with no diffusive terms (viscosity and conductivity are removed from the model). There is an analytical solution that can determine the shock, discontinuity, and left and right fan

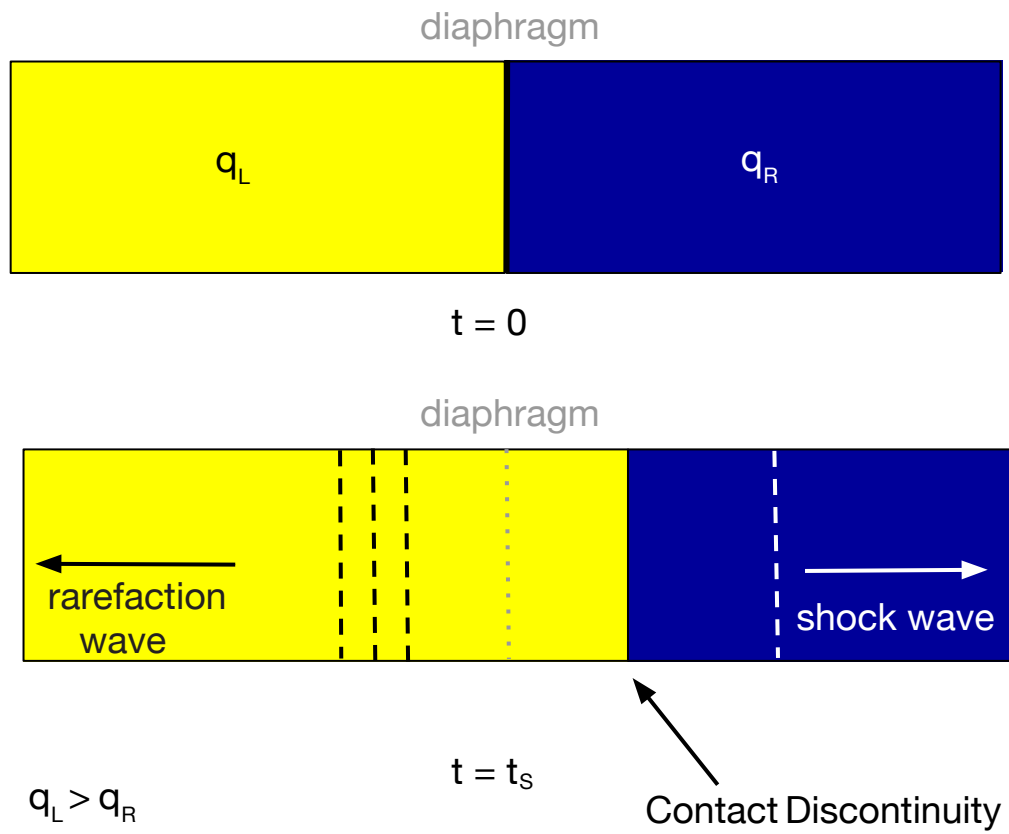


Figure 3.4: One-dimensional Sod test with initial conditions ($t = 0$) and after some time t_s . After $t = 0$, the diaphragm is ruptured and the gas with higher pressure q_L expands to the region of lower pressure q_R .

slopes. These can be determined with the use of initial conditions and their influence on other parameters in the system. Recall from Chapter 2 that

$$c_{(R,L)} = \sqrt{\frac{\gamma P_{(R,L)}}{\rho_{(R,L)}}},$$

where the subscripts (R, L) are used to represent the left and right portions of the tube. The slopes are consistent of linear equations that depend on a nonlinear relation known as the Rankine-Hugoniot condition. This condition is valid for the pressure jump across the shock

$$P = \frac{p_L}{p_R} \left[1 - \frac{(\gamma - 1)(c_R/c_L)(P - 1)}{\sqrt{2\gamma(2\gamma + (\gamma + 1)(P - 1))}} \right]^{2\gamma/(\gamma-1)}, \quad (3.35)$$

where P , the pressure jump across the shock is the variable of interest. The implicit function can be solved through root-approximation methods such as the Newton-Raphson method, or bisection method. The relations to determine their values are as follows

$$u_{\text{shock}} = u_R + c_R \sqrt{\frac{\gamma - 1 + (\gamma + 1)P}{2\gamma}}, \quad (3.36)$$

$$u_{\text{contact}} = u_L + \frac{2c_L}{\gamma - 1} \left[1 - \left(P \frac{p_R}{p_L} \right)^{\frac{\gamma-1}{2\gamma}} \right]. \quad (3.37)$$

The slopes of the regions of interest can be predicted with

$$x = x_0 + t \begin{cases} u_{\text{shock}} & \text{Shock wave} \\ u_{\text{contact}} & \text{Contact Discontinuity} \end{cases} \quad (3.38)$$

For our cases of interest, next, γ is a function of composition that is then tracked by the mass-fraction densities.

Table 3.1: Sod test simulation parameters for Riemann problem validation

Time Domain t	=	$[0,2]$
Tube's extent in grid x	=	$[-2,2]$
Spatial Resolution Δx	=	$3.33 \cdot 10^{-3}$
Temporal Resolution Δt	=	0.02
Left Domain Gas Properties q_L	=	$(1, 0, 3)^T$
Right Domain Gas Properties q_R	=	$(1, 0, 1)^T$

Application to Model

The model's performance can be tested when compared to the theoretical predictions made from the previous section. This will be conducted with the initial conditions:

$$q_L = \begin{pmatrix} \rho_L \\ u_L \\ p_L \\ Y_{1,L} \\ Y_{2,L} \end{pmatrix} = \begin{pmatrix} 3 \\ 0 \\ 3 \\ 0 \\ 0 \end{pmatrix}, \quad q_R = \begin{pmatrix} \rho_R \\ u_R \\ p_R \\ Y_{1,R} \\ Y_{2,R} \end{pmatrix} = \begin{pmatrix} 1 \\ 0 \\ 1 \\ 1 \\ 0 \end{pmatrix}$$

where the last parameter has been translated from E to p through the equation of state:

$$E = \frac{p}{\gamma - 1} + \frac{1}{2}\rho u^2.$$

The grid considered in this analysis has time $t = [0, 2]$ and the position $x = [-2, 2]$, with the membrane at $x_0 = 0$. Note: q_L and q_R are interchangeable such that the conditions presented can be reversed. The results of the Sod test Figures 3.5 - 3.7 give a contact and shock slope that matches with the predicted gas velocities with an error of less than 3%. Figures 3.6 - 3.7 demonstrate the modulation of atomic oxygen, a feature that can be calculated with the mass-fraction density method. Atomic oxygen is shown to modulate after both the shock and contact discontinuity speeds. This test was performed with several initial conditions and the performance of the model gave gas velocities within 5% of the predicted values. The error is

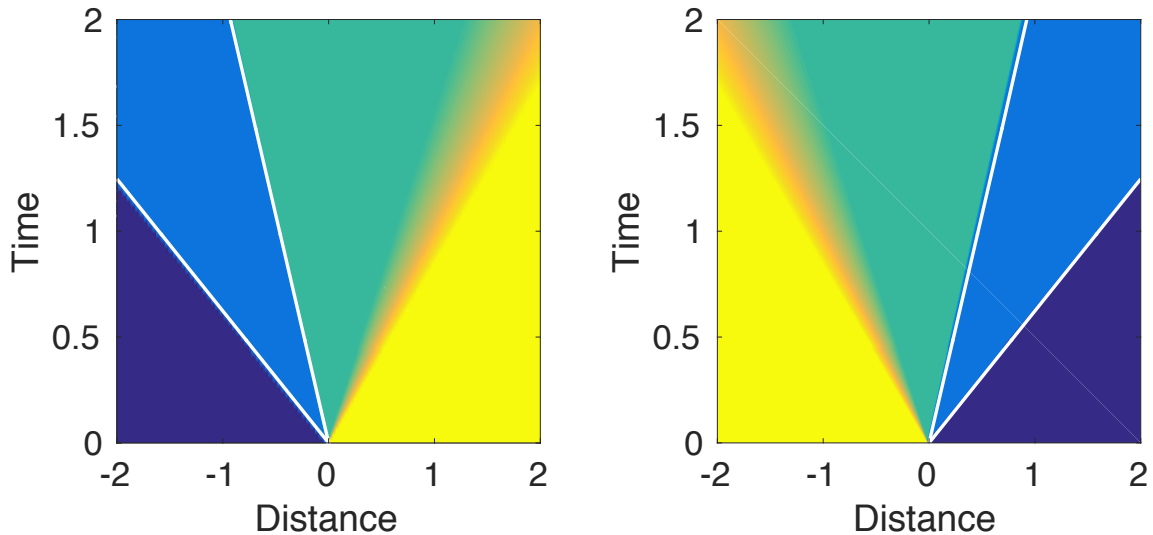


Figure 3.5: Sod test with shock wave and contact discontinuity labeled as white lines and calculated from the analytical solution. The results for initial conditions in Table 3.1 are shown in the left, while the reverse of Table 3.1 are shown on the right.

consistent despite atomic oxygen starting from the left or right side of the tube. In Sod [1978], several finite difference methods were surveyed, including the Godunov method. The error evaluated for the Godunov method was within 5%, which is a sign that the difference from theory in the mass-fraction density model is in part due to the numerical method. The mass-fraction density did not fall outside the permissible range of $Y_s \in [0, 1]$, which indicates the non-conservative mass-fraction model will remain within realistic values in this test.

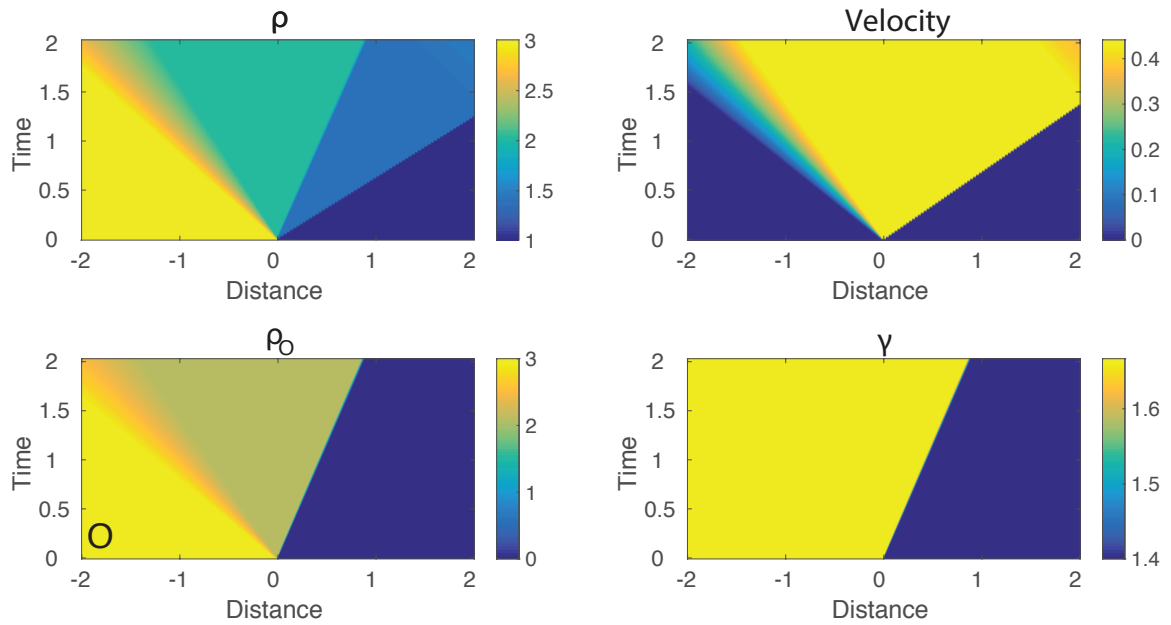


Figure 3.6: Parameters from the Sod test with the conditions found in Table 3.1, when atomic oxygen begins on the left.

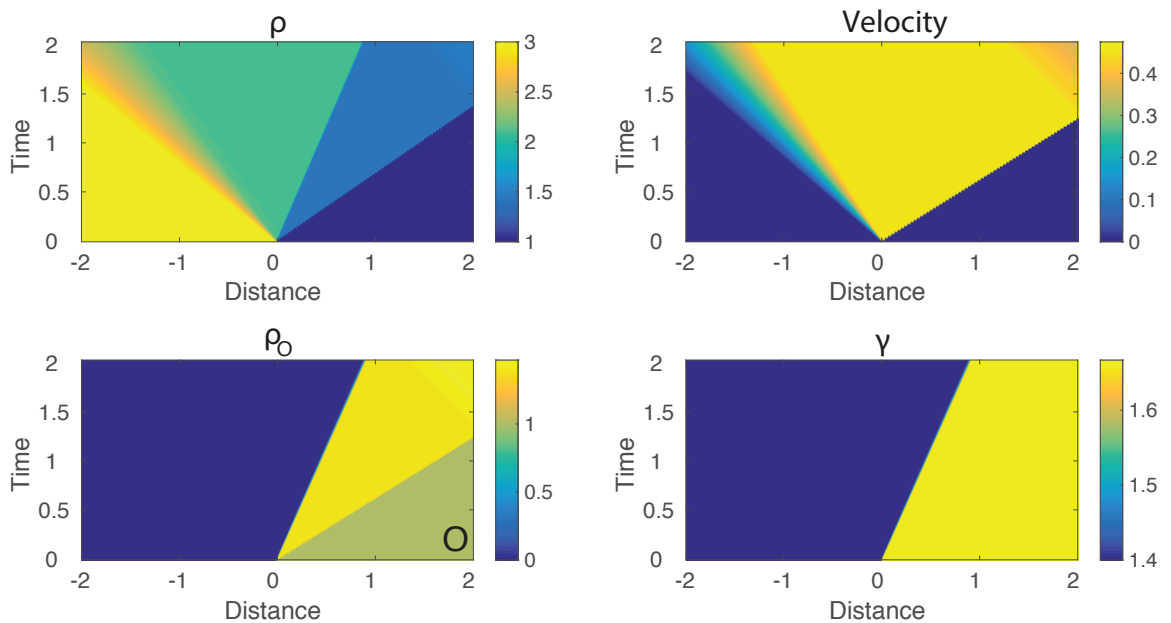


Figure 3.7: Parameters from the Sod test with the conditions found in Table 3.1, but q_L and q_R are reversed, when atomic oxygen begins on the left.

3.1.6 Chapter Summary

This chapter presented the numerical methods that are used to discretize the Euler equations and the diffusion equations that were developed in Chapter 2. CLAWPACK is used to solve the Euler equations, and the time-split diffusion equations are solved with an explicit forward in time, centered in space method, as opposed to an implicit method. A conservative and non-conservative mass-fraction density method was introduced in this section as an addition to the Euler equations. The results of using a conservative mass-fraction model nearly match the ones using a non-conservative mass-fraction model. Since the non-conservative model requires fewer computations to solve, that is the model that was chosen. The effects of a non-conservative mass-fraction model on the Riemann Solver used in Leveque's CLAWPACK were validated with the Sod test and via the case studies in Chapter 4.

Chapter 4

INVESTIGATIONS OF PARAMETER EFFECTS

4.1 Model Applicability and Extent

The purpose of this chapter is to investigate the properties of the mass-fraction density model outlined in this thesis by subjecting it to different test cases and comparing them to previously published work. The three cases studied are (1) the shock over the epicenter of the 2011 Tohoku Earthquake as reported by Zettergren et al. [2017]; (2) simulations of experimental results obtained from Mabie et al. [2016] compared to a 2D axisymmetric MAGIC model simulation; (3) and the shock source approximating the Misty Picture Experiment, as modeled by Sabatini et al. [2016]. These cases were chosen because they result in different spectra and amplitudes of vertically propagating waves to show how the model will behave when sources near the acoustic cut-off frequency, or sources with large amplitudes, are simulated. There are some physical limitations exhibited by one-dimensional models, which are seen through the comparison of the simulations and discussion. This section also shows the effects of compositional variation has on the characteristics of the atmosphere and acoustic wave propagation and the variability of the species as a function of the source amplitude and frequency, which can be enabled or disabled for each case study.

4.1.1 Tohoku Earthquake

Background and Setup

The 11 March, 2011 earthquake off the Pacific coast of Tohoku (Tohoku Earthquake), triggered powerful tsunami waves that reached heights up to 40.5 meters; until now, it is the most powerful earthquake recorded in Japan. The epicenter location was about 70 kilometers east of the Oshika peninsula of Tohoku, with an underwater hypocenter at around 29km deep Duputel et al. [2011]. The earthquakes began in a subduction zone, where one plate slides beneath another into the mantle which built up energy that was released in the form of an earthquake Duputel et al. [2011]. Several instruments were able to track the beginning and evolution of the earthquake, whose list includes seismometers (ocean bottom, or by land), GPS data, which observed crustal movements, earthquake related ionospheric perturbations, data from accelerogram, etc. Duputel et al. [2011]. The earthquakes impact the upper atmosphere first through vertical displacements of the Earth's crust or ocean surfaces which produce low-frequency acoustic (infrasound; periods 1-4 minutes) and gravity waves (periods > 5 min) Komjathy et al. [2013]. These waves can achieve significant amplitudes during upward propagation as the gases experience exponential velocity growth through the rarefied upper atmosphere, until dissipation dominates in the thermosphere. The ionospheric fluctuations, via ionospheric total electron content (TEC), can provide the basis for comparisons of models and experimental data. The atmosphere-ionosphere model in Zettergren et al. [2017] used a sinusoid in time, enveloped by a Gaussian in space as a simplified source of the disturbance. The source takes the form

$$v_z = A_s \sin(\omega t) \cdot (u_H(t) - u_H(t - t_w)), \quad (4.1)$$

where u_H refers to the Heaviside step function. The numerical parameters used in Equation 4.1 can be found in Table 4.1. The source was applied to the ground boundary condition as an imposed velocity which adds to the momentum term of the Euler equations. The rest of the boundary conditions terms were open with a scale term that was derived in Chapter 2, and applied to perturbations of the conservative

Table 4.1: Table of parameters and source characteristics for the Tohoku, or Zettergren et al. [2017] case study

Parameters	Description	Value
A_s	Source Amplitude	0.015m s^{-1}
t_w	Temporal Width	180s
ω	Angular Frequency	0.0349rad s^{-1}
t_c	Peak forcing time	0s
Δz	Spatial Resolution	100m
t_{max}	Simulation Duration	3600s

variables. The mass-fraction density of atomic oxygen and molecular oxygen were tracked during this simulation. From Equation 3.30, the remaining concentration of gas can be calculated which, for this study, is assumed to be molecular nitrogen.

Model Results

Figure 4.1 shows the general results of the one-dimensional simulation through wave properties and the mass fraction density. The perturbations seen in the mass-fraction density for oxygen are similar to the acoustic Mach number above 120 kilometers. This region holds the highest concentration of atomic oxygen, although the atmosphere is sparse. Since the source is strong, there is an opportunity for the waves to reflect from the atmosphere and the ground to create down-flows in addition to resonance. This can be seen through the perturbation in the Acoustic Mach Number at time $t = 20$ minutes at an altitude range of $z = 480 - 600$ kilometers. The source "turns off" after three minutes, so the oscillations that continue past the onset of the waves are caused by resonances that occur after a certain frequency is excited. Despite the strength of the source, the atomic oxygen mass fraction density remains numerically bounded by zero and unity. The atomic oxygen mass-fraction density is modulated at altitudes above 500 kilometers, and the variations can be seen in the atomic oxygen plotted in a logarithmic scale.

The 1D model gives comparable results to Zettergren et al. [2017] 2D model (above the source) seen in Figure 4.2. Two primary differences are the source amplitudes and

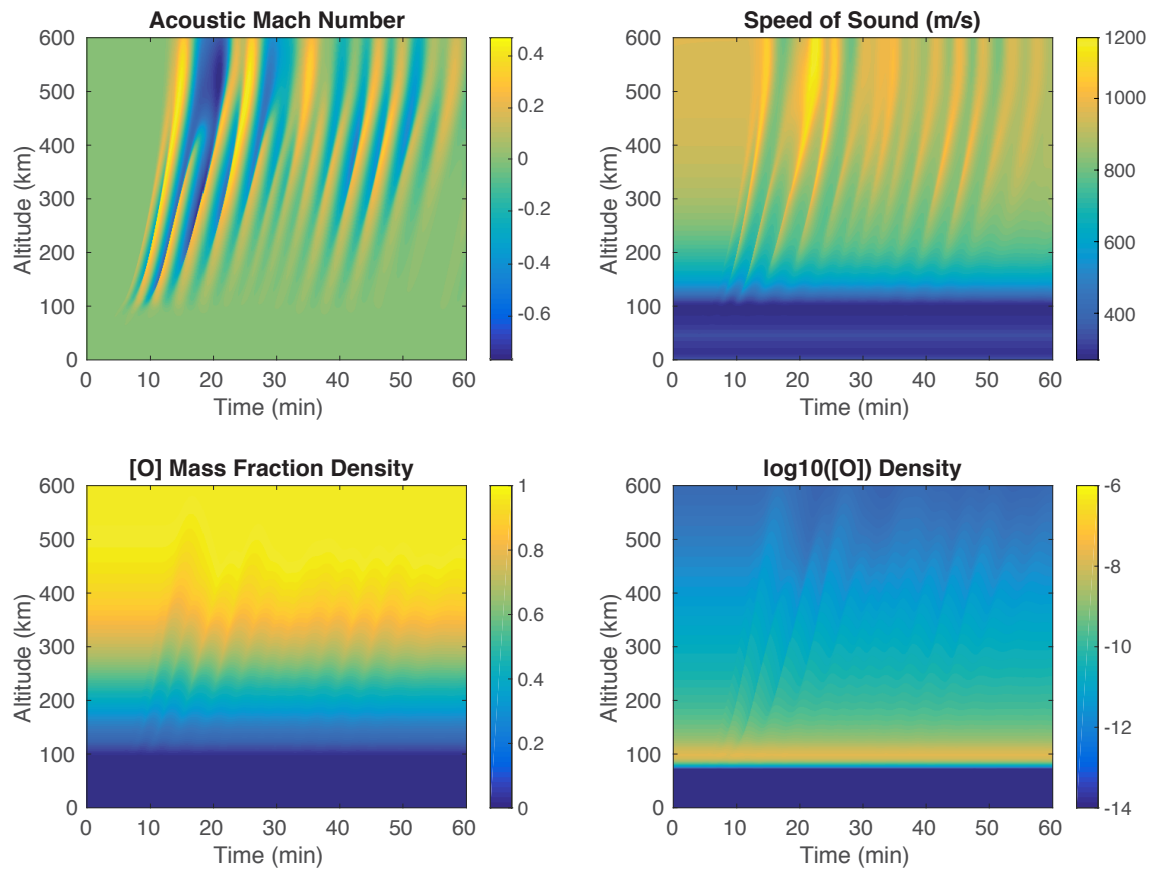


Figure 4.1: The acoustic Mach number (top right), speed of sound (top left), atomic oxygen mass fraction density (bottom left), and atomic oxygen in log scale (bottom right).

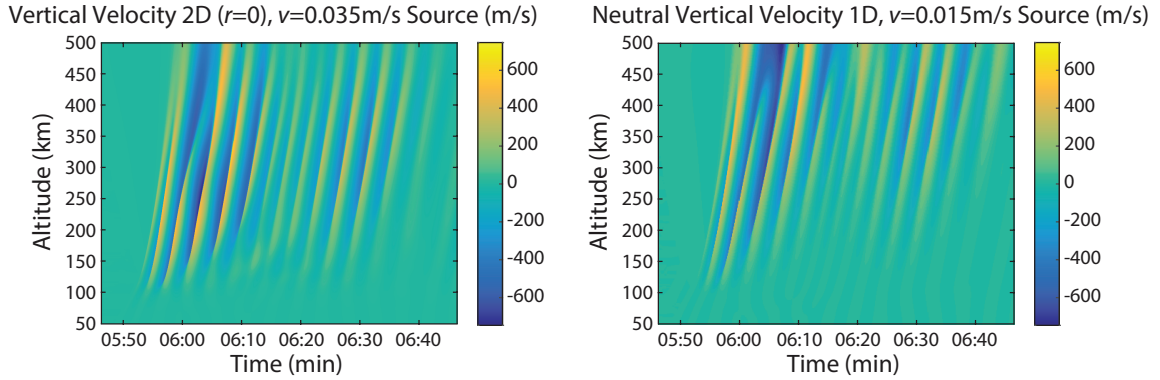


Figure 4.2: The velocity profile of a one-dimensional simulation of the Tohoku Earthquake as done by Zettergren et al. [2017] compared to the results of the 1D mass fraction density simulation (right).

the velocity at higher altitudes around the time of 6:05am as seen in Figure 9 of Zettergren et al. [2017]. The source amplitude for the 1D mass-fraction density simulation is about two times less than the one used in Zettergren et al. [2017] due to less geometric dispersion. Zettergren et al. [2017] also shows the effects of amplitude on the wave fronts at the source frequency. The 1D model is able to capture similar wave steepening, which can be seen through a parametric study that varied the frequency and duration of the source Figure 5.1. The simulation's dependence on amplitude, frequency, and resolution can highlight a physical limit to the 1D model. The 1D model saturates the wave field of the first arriving waves at lower source amplitudes (while preserving similar wave amplitude) than the 2D model when they run simulations at the same resolution. However, the cases in Figure 5.1 were run with the same amplitude but at a higher spatial resolution (100m), which resulted in more down flow.

The variations of composition can be seen in specific heat ratio in Figure 4.3. The amplitude of the source is strong enough to impact the specific heat ratio in both the onset of the source and the resonances that occur afterwards. The modulation of the specific heat appears to capture the strongest features of the vertically propagating acoustic wave. In the region of the strongest down-flow ($t = 20\text{min}$), the model varies the most with respect to the initialized profile, by a few percent. The variation is

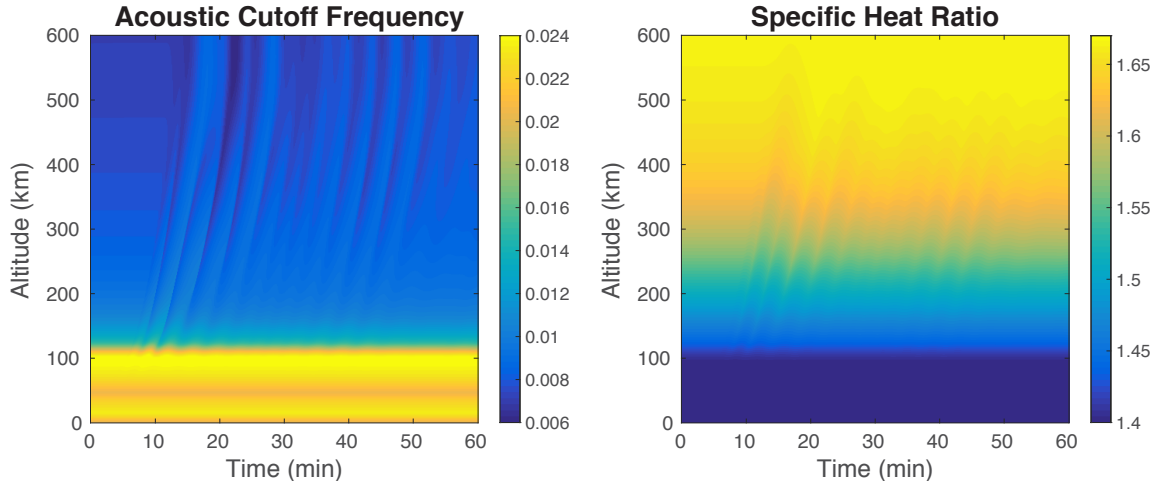


Figure 4.3: The variation in the acoustic cutoff frequency ω_A [rad/s] (left) and the specific heat ratio (right) due to the mass-fraction density model.

primarily dependent on the amplitude and frequency of the source.

4.1.2 Mabie et al. Rocket Launch

Background and Setup

One Antares rocket was launched from the Wallops Flight Facility (WFF) Mid-Atlantic Regional Spaceport on 9 January 2014 carrying a 1261 kilogram payload. Mabie et al. [2016] sought to investigate acoustic waves in the ionosphere to improve the understanding of energy transport from the lower to upper atmosphere using an advanced high-frequency radar (VIPR), to measure plasma displacements in the F region. These disturbances are usually identified by deformations in ionograms. Mabie et al. [2016] method allows for the detection of lower amplitude acoustic waves and provides basis for these disturbances to be modeled. Since the acoustic wave activity that resulted was less energetic than in the case of Tohoku, it was more difficult to observe in the integrated total electron content (TEC) data. For this case, a small spherically-symmetric forcing is specified at ground level, defined as $r = 0$. The rocket launch induced disturbance was modeled by a small amplitude Gaussian source with

open boundary conditions at the top of the domain and solid wall boundary conditions at the bottom of the domain ($r = 0$) to represent the ground. The source takes the form of Equation 4.2. The radial Gaussian envelope term at $r = 0$ that takes a similar form with spatial half-width.

$$F_s = A_s \exp \left(- \left[\frac{t - t_c}{\sqrt{2}t_w} \right]^2 - \left[\frac{r}{\sqrt{2}r_x} \right]^2 \right), \quad (4.2)$$

The value of the parameters used in this case study and their description can be found in Table 4.2.

Discussion

Figure 4.4 and Figure 4.5 show the resulting velocity evolution over the source compared to the MAGIC 2D cylindrical atmosphere model. The Figure 4.4 demonstrates the spherically symmetric 1D model is able to capture the acoustic waves similarly to the 2D cylindrical simulation. Similar to the Tohoku case, the amplitudes of the 1D simulation vs. the 2D are slightly less, but at low amplitudes, the difference is less since geometric dispersion is affected by the scale of the source, which in this case, is closer to a "point source". The results shown in Figure 4.5 show similar wave time scales and amplitudes to the data shown in Figure 4 of Mabie et al. [2016]. Here, a phase shift is revealed that is continued as altitude increases and time goes on. The 1D simulation shows the acoustic wave advancing faster than the 2D simulation which may be a result of the effects of compositional variation on the speed of sound,

Table 4.2: Table of parameters and source characteristics for the 1D simulation for the acoustic wave observations reported by Mabie et al. [2016]

Parameters	Description	Value
A_s	Source Amplitude	0.2 m s^{-2}
t_w	Temporal Width	7.5s
t_c	Peak forcing time	37.5s
Δr	Spatial Resolution	250m
t_{\max}	Simulation Duration	1200s
r_x	Spatial Half-Width	2km

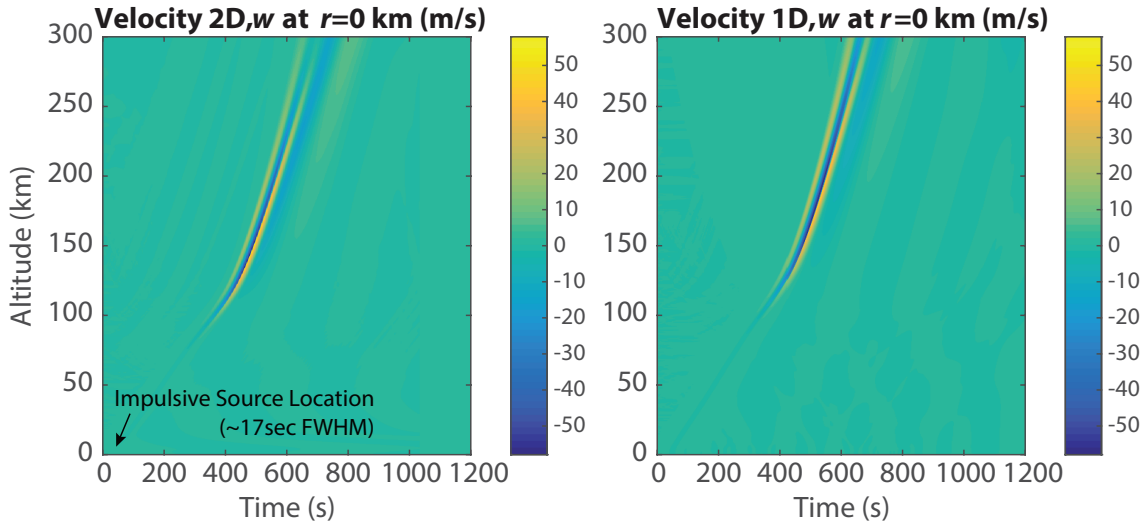


Figure 4.4: Velocity profiles as inspired by Mabie et al. [2016] observation of a rocket launch with the use of the 1D model (right) compared to the 2D (left) version of the MAGIC model.

or geometrical dispersion. The latter is the more likely of the two since the source amplitude is too weak to cause significant composition modulation (a variation of γ less than $10^{-5}\%$ difference for vertical wave velocities that achieve a maximum of 100 m/s or less). The vertical velocity calculated by the mass-fraction density, where composition is varied, also shows higher amplitudes as it propagates higher in the thermosphere. This phenomena is present in all of the cases done with this model. The effects of compositional variations for various sources of acoustic waves can be seen in Section 4.2.

The results of these models can help improve observations made in a similar way as Mabie et al. [2016] since they relied on numerical approximations to estimate the time of arrival of the acoustic wave to propagate from the ground to the altitude of the VIPR observation. Their calculations depended on approximate values for the speed of sound which is impacted by the composition variation. At the amplitudes reported by Mabie et al. [2016], the variations are negligible. However, if the source amplitude increases by an order of magnitude, compositional variations could impact the speed of sound, which would affect the interpretation of VIPR measurements in Mabie et al. [2016] algorithm.

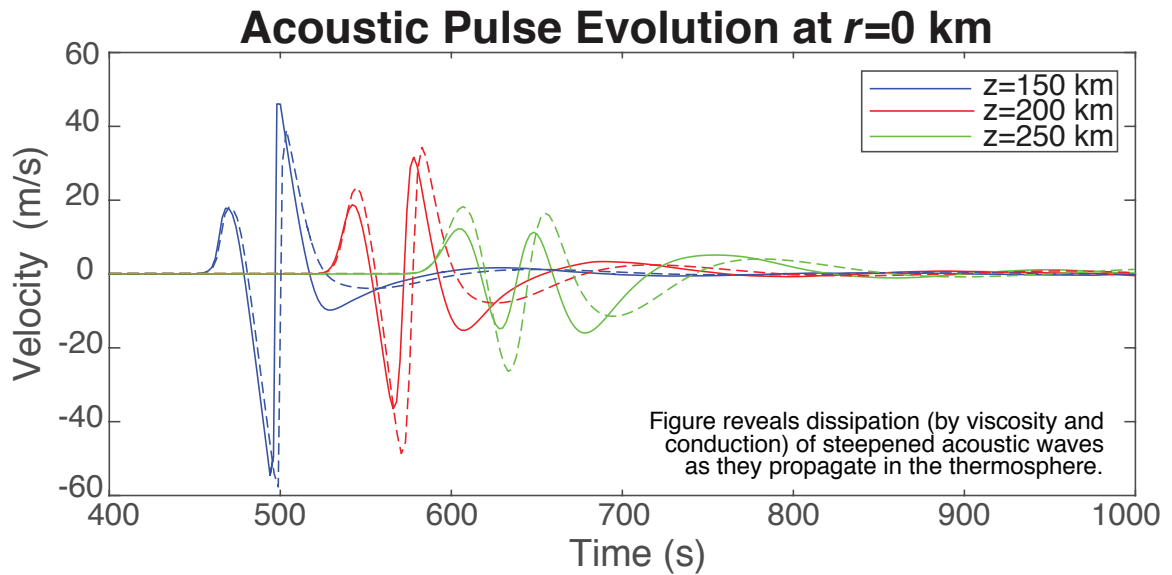


Figure 4.5: Velocity profiles as inspired by Mabie et al. [2016] observation of a rocket launch using 1D Mass Fraction Model (dashed) and the 2D/3D magic Cylindrical Simulation (solid), showing reasonable agreement.

4.1.3 Misty Picture Experiment

Background and setup

On 14 May, 1987, a test was conducted by the United States Defense Nuclear Agency (now the Defense Threat Reduction Agency), which involved the simulation of a small nuclear bomb through the detonation of 2125 kilograms of Ammonium Nitrate and Fuel Oil mixture into a 44-foot radius fiberglass hemisphere. The potential of the blast was the equivalent of 4 kilotons of TNT. The objectives of the test was to (1) provide an airblast, dust cloud, and ground shock environment for Department of Defense (DOD) sponsored experiments, and (2) provide a thermal environment for several experiments. The detonations provided a shock environment for which weapons shelter systems could be studied. The test was conducted at White Sands Missile Range, and was observed with a 60 barometric station network capable of detection a 1 kiloton yield explosion anywhere on the globe [Gainville et al., 2008].

The source used to numerically simulate this case was adopted from Sabatini et al. [2016]. Their work involved the characterization of the infrasonic source through the

Table 4.3: Table of source characteristics for the Misty Picture Experiment

Parameters	Description	Value
A_s	Source Scale	$2.5 \times 10^2 \text{ J m}^{-3} \text{ s}^{-1}$
b_s	Half Width of Source	600m
ω_s	Central Frequency	0.2π
T_s	Emission Duration	10s
Δ	Spatial Resolution	25m
Δt	Temporal Resolution	0.18s
t_{\max}	Simulation Duration	1800s
$(B_1, B_2, B_3, B_4, B_5)$	Altitudes of Interest	(5, 80, 120, 170, 90)km

analysis of overpressure and Energy Spectral Density (ESD). Overpressure refers to the sudden onset of a pressure wave after an explosion that travel near the speed of sound. The equation of the source and overpressure used for this study are shown below

$$\Lambda(z, t) = \frac{\mathcal{A}_s}{2} \begin{cases} \sin(\omega_s t) \left[1 - \cos(\omega_s t) \exp\left(-\frac{\log(2)z^2}{b_s^2}\right) \right] & t \in [0, T_s] \\ 0 & \text{otherwise} \end{cases} \quad (4.3)$$

$$\Phi(z, t) = \frac{p(z, t) - \bar{p}(z)}{\mathcal{A}_s \sqrt{\bar{\rho}(z)}}, \quad (4.4)$$

where Λ refers to the forcing term that is added to the energy equation, \mathcal{A}_s is the source strength in ($\text{J m}^{-3} \text{ s}^{-1}$), ω_s is the central frequency in (Hz), b_s is the half-width of the source in (m), and $\Phi(z, t)$ refers to the overpressure as defined by Bergmann [1945]. The parameters that define the setup of the experiment are shown in Table 4.3. The boundary conditions were the solid wall for the bottom boundary and an open top boundary. In order to match Sabatini et al. [2016]’s Cartesian 2D simulation, cylindrical symmetry was implemented in the mass-fraction density model. A key difference between the analysis is the speed of sound profile that was calculated with the use of a spline in Sabatini et al. [2016] whereas in the 1D model, it is calculated with the use of the atmospheric properties from the day and time of the experiment as projected from NRLMSISE-00 [Picone et al., 2002].

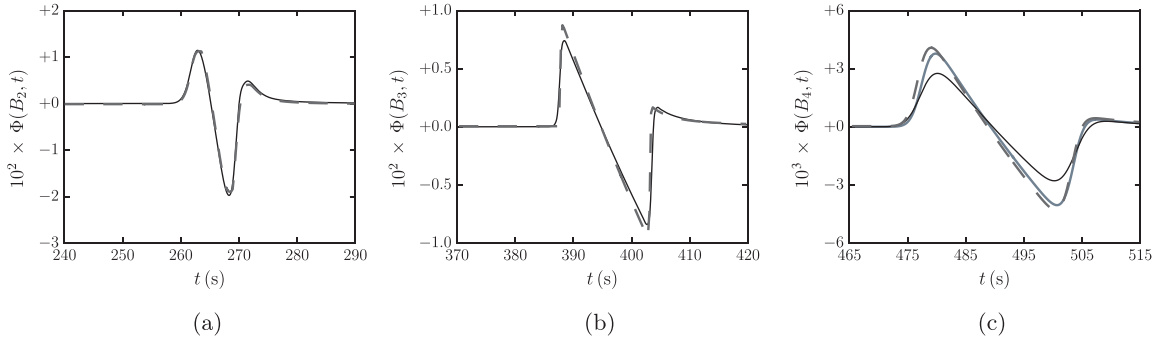


Figure 4.6: Results of nonlinear Misty Picture run from Sabatini et al. [2016] (dark solid line) with the results of the 1D mass fraction density model with (dashed grey line) compositional variation superimposed with the same scale. The solid slate grey line (c) shows a run with no compositional variation.

Discussion

The overpressure at various altitudes are shown in Figure 4.6. The simulation results match those of Sabatini et al. [2016] with a similar amplitude effect exhibited in the previous case study. The amplitude shift seems to favor the acoustic velocity in higher altitudes which might be indicative of the 1D model's impact of the atomic oxygen mass fraction density on the speed of sound. The linear cases studied in Sabatini et al. [2016] show the importance of viscous and thermal terms since the N-wave from the nonlinear case does not show up in the linear case. The differences from the 1D model and Sabatini et al. [2016] in Figure 4.6 can be due to a variety of factors. In the 1D simulation, acceleration due to gravity, specific heat ratio, and specific gas constant (R) are altitude dependent whereas they are constant in Sabatini et al. [2016]. The diffusive terms are also treated differently which could influence the wave propagation. The Prandtl number was fixed to $Pr = 0.72$ whereas the one used in the 1D model is based on the actual composition.

To assess the numerical accuracy of the 1D mass-fraction density model, an N-wave at 90km is analyzed at different spatial resolutions. Sabatini et al. [2016] conducted a similar study with $\Delta z = 75, 100, 125, 150\text{m}$ and found convergence for the first two lobes of the energy spectral density (ESD) which have most of the signals energy. The higher frequencies exhibit larger variations from the higher resolution cases than

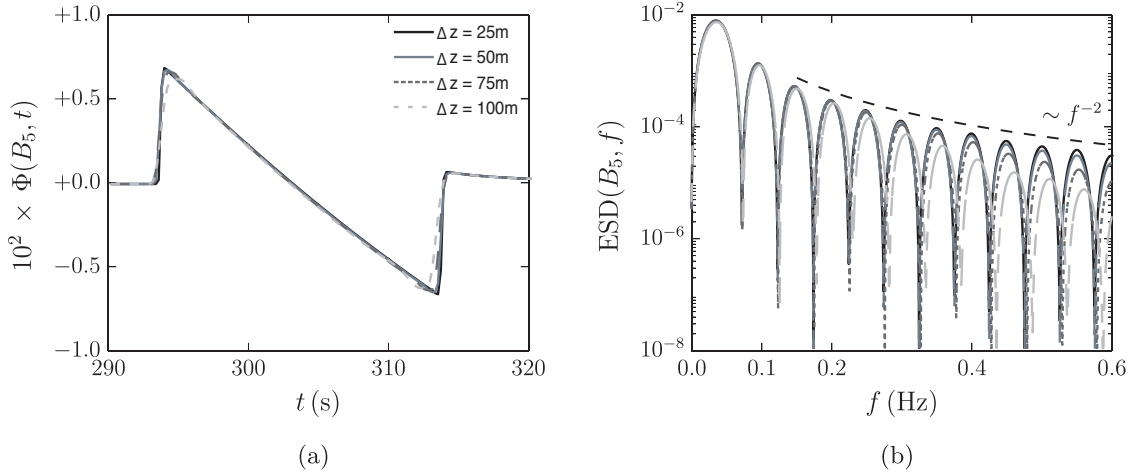


Figure 4.7: Temporal signal at 90km (a) and the One-Sided energy spectral density obtained at different spatial resolutions (b). The plot shows reasonable agreement with Figure 16 in Sabatini et al. [2016].

the lower ones which was expected. The maxima of the ESD spectrum display a f^{-2} behavior similar to the one shown in Figure 4.7. The ESD produced by the 1D model shows a phase shift at the higher frequencies which may be due to the inability to resolve the wavelength with enough points as the frequencies get higher. In addition, the method used in this thesis is second order accurate while Sabatini et al. [2016] used a fourth order method. However, for the higher resolution cases, the maxima line up.

4.2 Effects of Compositional Variation

The analysis presented in previous sections have compared previously published work with the results of the 1D mass-fraction density model. The differences between the models can be a result of the higher-dimensional model's ability to account for physical dispersion and refraction processes that are not included in a 1D model. To further characterize the mass-fraction density model simulations, the case studies above are studied with and without compositional variation. When discussing species

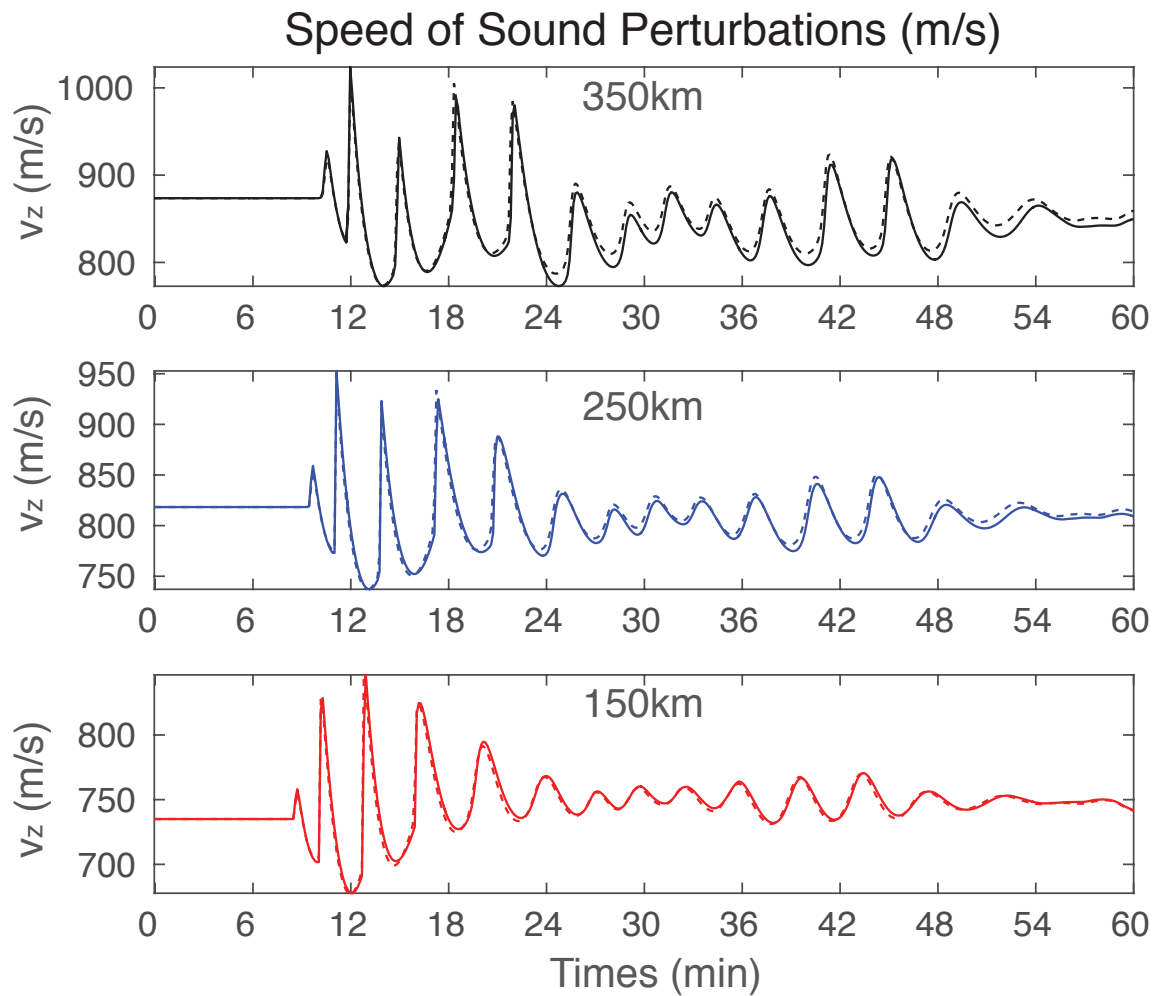


Figure 4.8: Speed of sound perturbations from a source similar to the 2011 Tohoku simulation at three heights. The dashed and solid lines represent the speed of sound calculated with and without specific heat ratio variation respectively.

modulation, two parameters that affect wave propagation the most are the specific heat ratio (γ) and the specific gas constant. These parameters affect the speed of sound which then affects the wave velocity v_z and other parameters such as the vertical wave number (k_z).

From the case studies above, it is reasonable to assume compositional variation has an effect on the phase and amplitude of an acoustic wave with large amplitude and low frequency, such as the ones shown in Figure 4.8. Here, compositional variations cause the speed of sound to vary within two percent of that calculated without compositional variation. Stronger variations are found as the wave propagates higher in the atmosphere, as the source amplitude increases, and the frequency approaches the acoustic cut-off frequency. This is likely due to the speed of sound modulations which are affected more dramatically as the source term gets stronger. Compositional variation increasing with amplitude is reasonable since it is a nonlinear function of the vertical velocity which is affected by the source.

The *Misty Picture* and Mabie et al. [2016] Rocket launch cases involve smaller amplitudes and higher frequencies than the Tohoku case which makes the effects of compositional variation less noticeable. For the Rocket Launch case, the compositional modulation of γ varied by a maximum of 0.1% which affected the velocity by a similar quantity, seen in Figure 4.9. At the top of Figure 4.9 is Figure 4.10 the rocket launch case with a source amplitude at ten times the original value. The effects of modulation are seen around the area where the amplitude of the velocity is greatest. The effects of the variations in composition in this case seem to dampen the vertical velocity and shift the velocity out of phase. A similar effect can be seen in Figure 4.8 at 150km. The differences in the velocities are small enough such that it can be considered negligible. Similar to Figure 4.6, Figure 4.11 shows the work of Sabatini et al. [2016] and the 1D model results with and without compositional modulation. At the lower altitudes B_2 , match in terms of how smooth the overpressure is and in the decrease of the waves amplitude relative to the sources initial strength. As the wave propagates towards the thermosphere, an N-wave is formed and at higher altitudes, the wave period increases. With the variation in composition, the modulation matches the results of Sabatini et al. [2016] better than without, however this is

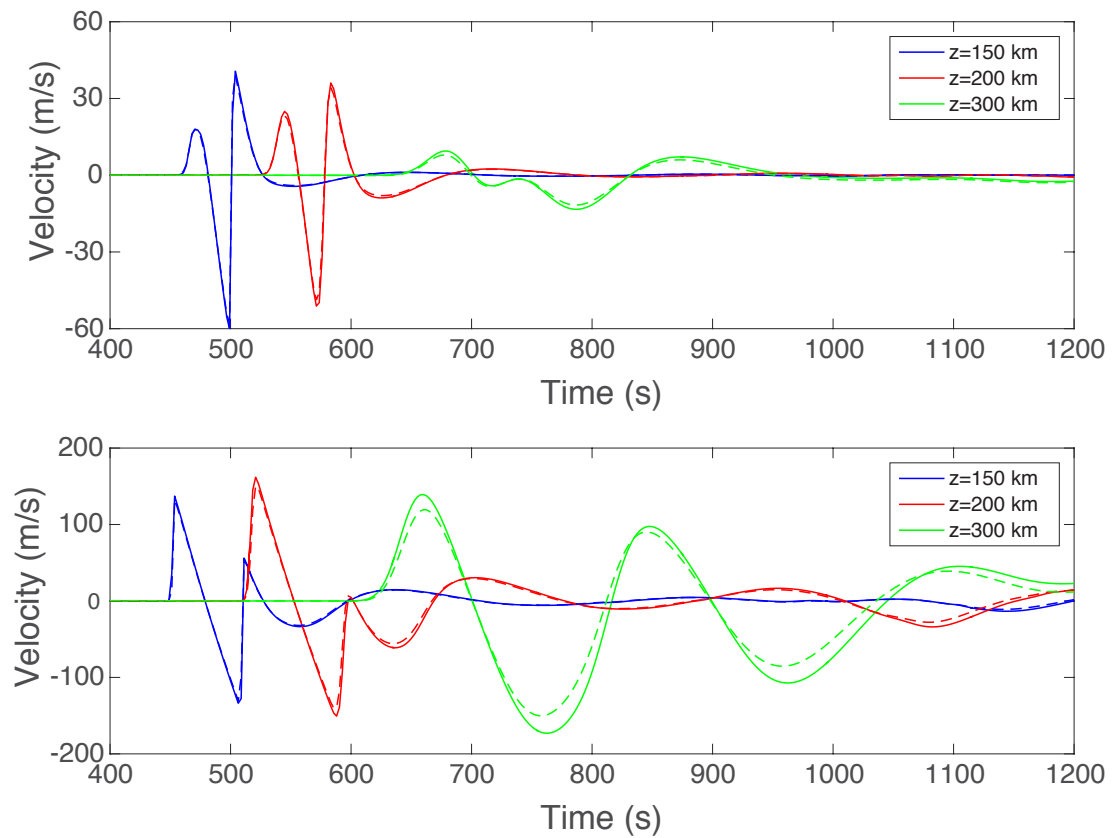


Figure 4.9: Velocity of acoustic wave for the simulation inspired by the results of Mabie et al. [2016]. The dashed lines are with compositional variation and the solid lines are without. The top shows the run with parameters from Table 4.2, and the bottom shows the same run with a source amplitude of ten times the one of the top run.

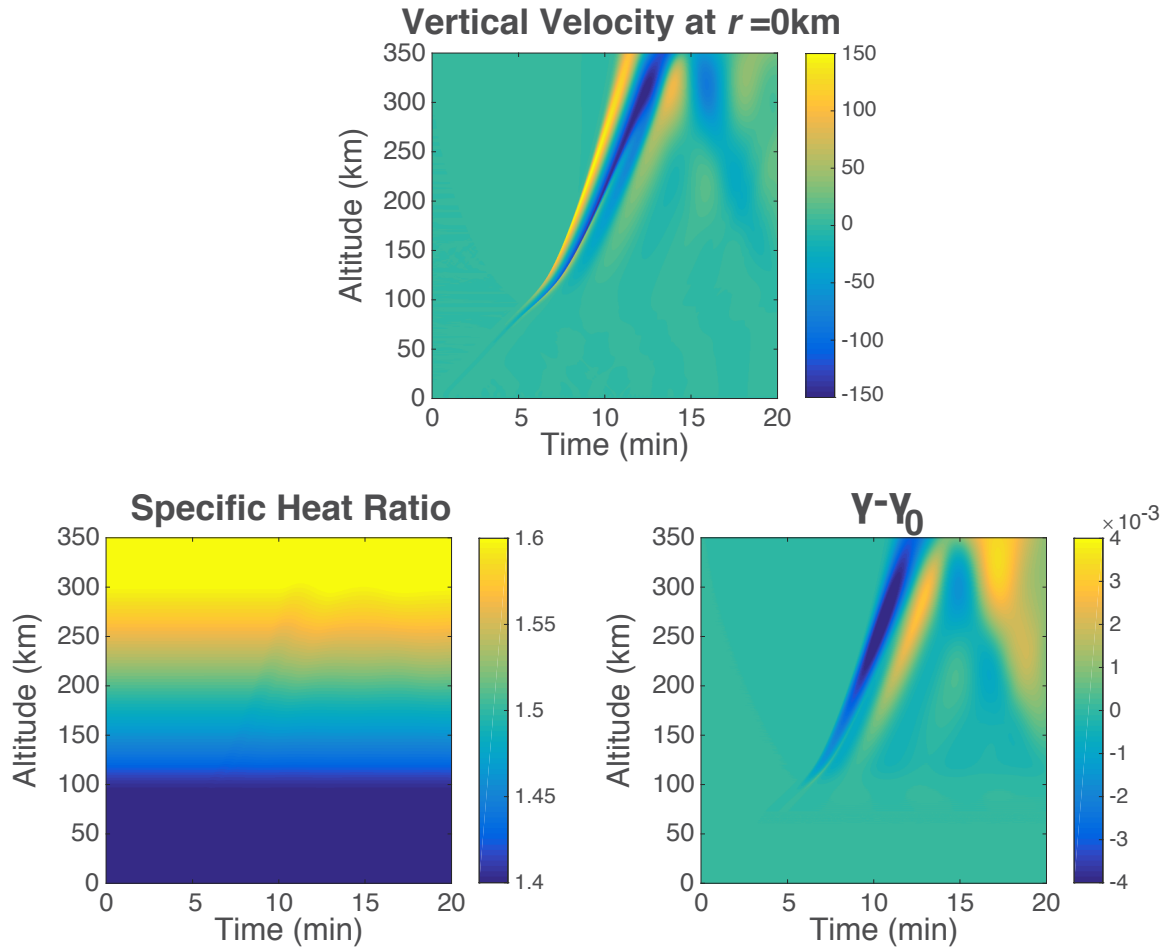


Figure 4.10: The Rocket Launch run with ten times the source amplitude as the parameters in Table 4.2. The difference between the varying specific heat ratio and the profile when the specific heat is constant.

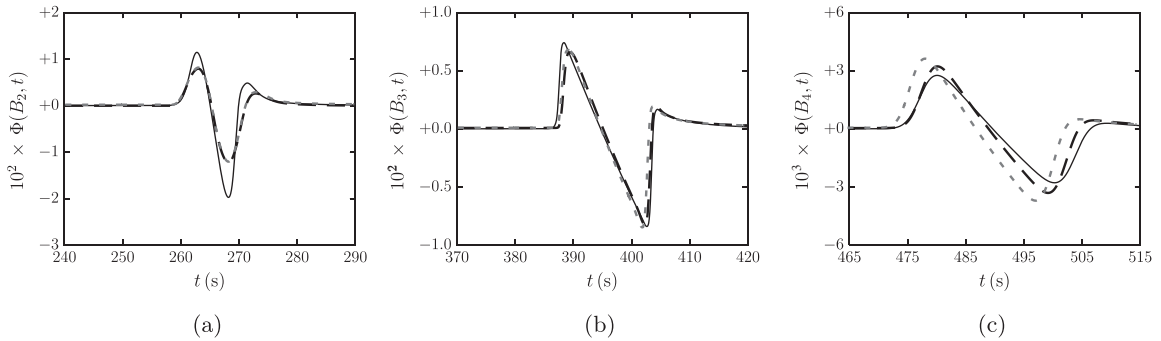


Figure 4.11: Results of misty picture run with the same parameters from Table 4.3, but with a resolution of $\Delta z = 100\text{m}$. Sabatini et al. [2016] run is shown in (dark solid line) with the results of the 1D mass-fraction density with compositional variation (dashed gray line) and without variation (dashed black line).

fortuitous since Sabatini et al. [2016] did not include compositional variation. This indicates that species modulation does affect propagation, especially in the thermosphere, and does modify the amplitude and arrival time of the acoustic wave. The resolution for this run was increased and the result shows an wave that is shifted from Sabatini et al. [2016]. The variations in this case were similar to the ones in the Rocket Launch case, so the shift in phase could be a result of the method being more diffusive at coarser resolutions.

4.3 Chapter Summary

The 1D mass fraction model underwent three case studies that sought to explore its properties. In large amplitude simulations and in cases where the frequency approached the acoustic cut-off limit, the model remained stable. The effects of compositional variation were explored through a comparison of the same case studies simulated with and without species modulation. The results of this show species modulation is prevalent at altitudes greater than 200km, but at small enough amplitudes to where the approximation is reasonable.

Chapter 5

SUMMARY AND SUGGESTIONS FOR FUTURE WORK

5.1 Summary

One-dimensional models have several important uses, including studies that involve parametric sweeps of atmospheric parameters to determine their influence on acoustic waves in the atmosphere, and assessing the feasibility of running higher dimensional simulations. The former is the basis of several studies and is usually done with 1D models since they are computationally inexpensive. There exist numerous parametric studies that can be investigated with the model developed in this thesis; one study that will be suggested below: Acoustic responses that do and do not exhibit resonances.

5.2 Conclusion

This thesis covers the development and validation of a nonlinear compressible atmospheric acoustics model that tracks mass-fraction densities of species. The model was developed through the addition of a mass fraction density equation that is advected along with the compressible Euler equations. The Euler equations are solved with the use of CLAWPACK that applies finite volume methods to numerically solve the

Euler equations through f-wave methods, as introduced in Bale et al. [2003]. The Euler equations do not include the diffusive terms, molecular viscosity, and thermal conductivity, so they are solved through a time-split solution through an explicit forward-in-time-centered-in-space method of parabolic equations.

The 1D mass-fraction density developed showed little difference between its conservative and non-conservative forms such that the non-conservative form was used since it involves less calculations. Both cases had mass-fractions that remained within physical limits, regardless of the geometry of the problem. The results of the two models are similar for problems that involve multi-dimensional symmetry. The model was validated through the use of a Sod test whose results showed similar results when compared to the analytical solutions of the problem.

The model was tested through three cases of that varied in geometry, and source amplitude through the use of symmetrical symmetry. It demonstrated its ability to retain stability when it simulated the strong shock caused by the 2011 Tohoku Earthquake. It was able to resolve smaller amplitude sources that involve high resolution simulations in weaker sources such as the Misty Picture Experiment Sabatini et al. [2016]. Since the model is one-dimensional, it is able to capture these processes above the source, although multi-dimensional solvers achieve more accurate results at greater cost. However, this model was able to produce similar results along with the compositional variation. The compositional variations this model produces have a small but measurable impact on the propagation of the wave. The speed of wave propagation and its amplitude are affected due to their dependence on the compositionally dependent parameters such as the ratio of specific heat, viscosity, and thermal conductivity. The areas that are most affected are the ones that are above the mesosphere, due to presence of atomic oxygen.

5.3 Future Work

5.3.1 Parametric Resonance Study

Acoustic wave pulses that propagate and evolve through the atmosphere have potential to become trapped between the ground and the lower thermosphere, depending on the spectrum of the source that produced them, which can cause acoustic modal resonances. Impulsive disturbances such as the 2011 Tohoku earthquake caused by vertical movement of the ocean surface, contain frequencies that excite resonances in the atmosphere whereas higher frequency events, such as the rocket launch reported by Mabie et al. [2016] do not. These resonances have been numerically investigated Matsumara et al. [2011], and confirm that acoustic resonance should be present following events that can excite them. By contrast, results by Chum et al. [2016] suggest that higher frequency sources generate waves that are more likely to nonlinearly steepen and dissipate, evolving into a shock-like "N-wave" pulse. Signatures reported by Li et al. that followed from the 2016 Kaikoura earthquake event identify intermediate behavior of the atmosphere, including both steep wave and persistent oscillatory features interpreted to be a result of complex multi-fault structure of the earthquake.

Two regimes of acoustic responses – those that do and do not exhibit excited resonances - can be distinguished through a series of parametric simulation case studies. Acoustic response regimes can be investigated for sources of varied spectral content and amplitude. An example of this is shown in Figure 5.1. The source used for this search is the same as the one used in the 2011 Tohoku case study. Two parameters were changed, the angular frequency and the temporal width of the source. From this study, most waves experience the initial steepened acoustic wave, but the higher frequencies with lower temporal width exhibit less resonance such as the case with $t_w = 18\text{s}$ and $\omega = 0.35\text{rad/s}$. Results from a study like this could suggest that the presence (or absence) of measured resonances can provide insight into the spectral characteristics of unknown sources.

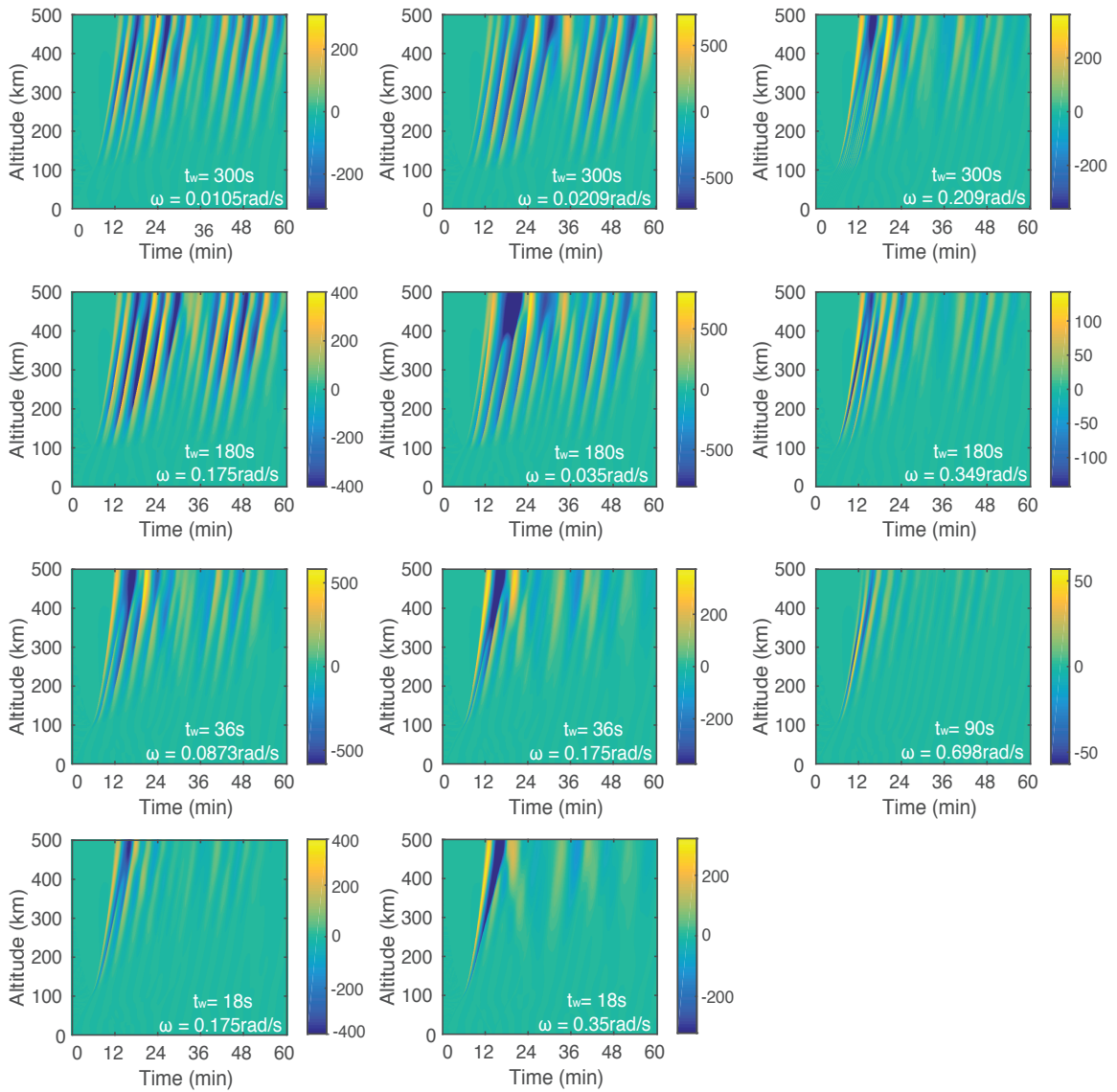


Figure 5.1: An example of a potential parametric study that changes the frequency and envelope of a source to provide insight into spectral characteristics of unknown sources.

5.3.2 Future Model Additions

Mass Diffusion

The solutions to the diffusion equations use an explicit scheme which consumes a lot of the time to ensure stability and accuracy. There are other implicit FDM schemes, such as the trapezoidal rule, backwards differentiation formula (TRBDF), which are more accurate and could require less computations. These solvers can also be optimized with the use of parabolic equation speed-up algorithms known as Super-Time-Stepping (STS) schemes. The algorithm can cut down the time it takes to solve the diffusion terms.

Additionally, the effects of mass diffusion were not included but could be included as a source term for the mass-fraction equations. Consider the mass-fraction density equations in one dimension with a source Z_s such that:

$$\frac{\partial Y_s}{\partial t} + u \frac{\partial Y_s}{\partial x} = Z_s, \quad (5.1)$$

with

$$Z_s = R_s - \frac{1}{\rho} \frac{\partial J_s}{\partial x}. \quad (5.2)$$

where R_s is the production of species s , such as by relaxation processes, and J_s is the diffusive mass-flux vector [Scott et al., 2017]. Including the effects of the species diffusion could lead to a more complete model that has species interaction with one another, that would produce similar results to a true multifluid, but at lower cost. This may also help with simulations involving other wave dynamics.

Bibliography

- R. Abgrall and S. Karni. Computations of compressible multifluids. *Computational Physics*, 169:594–623, 2000.
- E. L. Afraimovich, E. A. Kosogorov, L. A. Leonovich, N. P. Palamartchouk, K. S. Perevalova, and O. M. Pirog. Determining parameters of large-scale traveling ionospheric disturbances of auroral origin using gps-arrays. *Elsevier*, 62(7):553–565, May 2000.
- C. E. Anderson. *Cumulus Dynamics*. Pergamon Press, New York, 1960.
- J. Artru, T. Farges, and P. Lognonne. Acoustic waves generated from seismic surface waves: propagation properties determined from doppler sounding observations and normal-mode modelling. *Geophysical Journal International*, 158(3):1067–1077, September 2004.
- J. Artru, V. Ducic, P. Kanamori, H. Lognonne, and M. Murakami. Ionospheric detection of gravity waves induced by tsunamis. *Geophysical Journal International*, 160(3):840–848, March 2005.
- D. M. Baker and K. Davies. Waves in the ionosphere produced by nuclear explosions. *Department of Energy, Office of Non-Proliferation and National Security*, 73(1):448–451, January 1968.
- D. Bale, R. Leveque, S. Mitran, and J. Rossmannith. A wave propagation method for conservation laws and balance laws with spatially varying flux functions. *Society for Industrial and Applied Mathematics*, 24(3):955–978, 2003.

- P.M. Banks and G. Kockarts. *Aeronomy*. Academic Press, 1973.
- P. G. Bergmann. The wave equation in a medium with a variable index of refraction. *The Journal of Acoustical Society of American*, 17(4):329–333, November 1945.
- E. Blanc. Observations in the upper atmosphere of infrasonic waves from natural or artificial sources: A summary. *Annales Geophysicae*, 3(6):673–687, January 1985.
- E. Calais and J. B. Minster. Gps detection of ionospheric perturbations following the january 17, 1994, northridge earthquake. *Geophysical Research Letters*, 22(9):1045–1048, May 1995.
- G. Chimonas and W. R. Peltier. On severe storm acoustic signals observed at ionospheric heights. *Journal of Atmospheric and Terrestrial Physics*, 36(5):821–828, May 1974.
- J. Chum, M. A. Cabrera, Z. Mosna, M. Fagre, J. Base, and J. Fiser. Nonlinear acoustic waves in the viscous thermosphere and ionosphere above earthquake. *Journal of Geophysical Research: Space Physics*, 121(12):11,585–12,246, December 2016.
- J. B. Davies and C. Archambeau. Simulation of atmospheric and ionospheric disturbances due to gravity waves from near-surface sources. *Journal of Atmospheric and Terrestrial Physics*, 1994.
- A. D. Del Genio, J. M. Straus, and G. Schubert. Effects of wave induced diffusion on thermospheric acoustic gravity waves. *Geophysical Research Letters*, 5(4):265–267, April 1978.
- J. J. Dudis and C. A. Reber. Composition effects in thermospheric gravity waves. *Geophysical Research Letters*, 3(12):727–730, December 1976.
- Z. Duputel, L. Rivera, H. Kanamori, and G. Hayes. W phase source inversion for moderate to large earthquakes. *Geophysical Journal International*, 189(2):1125–1147, 2011.

- T. Farges, E. Blanc, A. Le Pichon, T. Neubert, and T. H. Allin. Identification of infrasound produced by sprites during the sprite2003 campaign. *Geophysical Research Letters*, 32(1):1813–1817, January 2005.
- O. Gainville, P. Blanc-Benon, E. Blanc, R. Roche, C. Millet, F. Le Piver, B. Despres, and PF Piserchia. Misty picture: A unique experiment for the interpretation of the infrasound propagation from large explosive sources. *The Journal of Acoustical Society of America*, 123(5):3829–3829, 2008.
- M. Garces, M. Willis, C. Hetzer, A. Le Pichon, and D. Drob. On using ocean swells for continuous infrasonic measurements of winds and temperature in the lower, middle, and upper atmosphere. *Geophysical Research Letters*, 31(19):19304–19308, October 2004.
- E. E. Gossard and W. H. Hooke. *Waves in the Atmosphere Infrasound and Gravity Waves*. Elsevier Science Ltd, 1975.
- M. P. Hickey, G. Schubert, and R. L. Walterscheid. Acoustic wave heating of the thermosphere. *Journal of Geophysical Research*, 106(A10):21543–21548, October 2001.
- M. P. Hickey, R. L. Walterscheid, and G. Schubert. A full-wave model for a binary gas thermosphere: Effects of thermal conductivity and viscosity. *Journal of Geophysical Research Letters*, 120:3074–3083,, March 2015.
- C. O. Hines. Internal atmospheric gravity waves at ionospheric heights. *Canadian Journal of Physics*, 72(17):4559–4576, September 1960.
- C. O. Hines. Dynamical heating of the upper atmosphere. *Journal of Geophysical Research*, 70(1):177–183, January 1965.
- D. P. Kanellakos. Response of the ionosphere to the passage of acoustic gravity waves generated by low altitude nuclear explosions. *Journal of Geophysical Research*, 72(17):4559–4576, September 1967.

- V.D. Karlov, S.I. Kozlov, and G.N. Tkachev. Large-scale disturbances of the ionosphere occurring during the flight of a rocket with a working engine. *Kosmicheskie Issledovaniia*, 18:266–277, March 1980.
- H. King, J.W. and Kohl. Upper atmospheric winds and ionospheric drifts caused by neutral air pressure gradients. *Nature*, 2006:699–701, May 1965.
- A. Komjathy, D. A. Galvan, P. Stephens, M. D. Butala, V. Akopian, B. Wilson, O. Verkhoglyadova, A. J. Mannucci, and M. Hickey. Detecting ionospheric tec perturbations caused by natural hazards using a global network of gps receivers: The tohoku case study. *Earth, Planets and Space*, 64(12):24, Jan 2013. ISSN 1880-5981.
- V. Krasnov, Y. A. Drobzheva, and J. Lastovicka. Acoustic energy transfer to the upper atmosphere from sinusoidal sources and a role of nonlinear processes. *Journal of Atmospheric and Solar-Terrestrial Physics*, 69(12):1357–1365, August 2007.
- A. Le Pichon. Acoustic propagation and atmosphere characteristics derived from infrasonic waves generated by the concorde. *The Journal of the Acoustical Society of America*, 111(1):629–641, July 2002.
- A. Le Pichon, E. Blanc, and D. Drob. Probing high-altitude winds using infrasound. *Journal of Geophysical Research*, 110(D20104):1–4, October 2005.
- A. Le Pichon, L. Ceranna, C. Pilger, P. Mialle, D. Brown, P. Herry, and N. Brachet. The 2013 russian fireball largest ever detected by ctbto infrasound sensors. *Geophysical Research Letters*, 40(14):3732–3737, March 2013.
- Randall J. LeVeque. *Finite-Volume Methods for Hyperbolic Problems*. Cambridge University Press, 2002.
- J. Mabie, T. Bullett, P. Moore, and G. Vieira. Identification of rocket induced acoustic waves in the ionosphere. *Geophysical Research Letters*, 43(20):11024–11029, October 2016.

- M. Matsumara, A. Saito, T. Iyemori, H. Shinagawa, T. Tsugawa, Y. Otsuka, M. Nishioka, and C. H. Chen. Numerical simulations of atmospheric waves excited by the 2011 off the pacific coast of tohoku earthquake. *Earth, Planets and Space*, 23:2177–2180, September 2011.
- J. M. McKisic. Infrasound and the infrasonic monitoring of atmospheric nuclear explosions: A literature review. *Department of Energy, Office of Non-Proliferation and National Security*, 1(1):1–321, February 1997.
- J. W. Meriwether, J. L. Mirik, A. Biondi, F. A. Herrero, and C. S. Fesen. Evidence for orographic wave heating in the equatorial thermosphere at solar maximum. *Geophysical Research Letters*, 23:2177–2180, 1996.
- P. M. Nagorsky. The inhomogeneous structure of the ionospheric f-region produced by rockets. *Geomagnettizm i aeronmiya*, 38:100–106, 1998.
- P. M. Nagorsky. Analysis of the hf radio signal response to ionospheric plasma disturbances caused by shock acoustic waves. *Izvestiya VUZov, RadioEzika*, 42:32–44, 1999.
- W. R. Peltier and C. O. Hines. On the possible detection of tsunamis by a monitoring of the ionosphere. *Journal of Geophysical Research*, 81(12):1995–2000, April 1976.
- A. L. Pichon, E Blanc, and A Hauchecorne. *Infrasound Monitoring for Atmospheric Studies*. Springer Science and Business Media, 2010.
- J. M. Picone, A. E. Hedin, D. P. Drob, and A. C. Aikin. Nrlmsise-00 empirical model of the atmosphere: Statistical comparisons and scientific issues. *Journal of Geophysical Research: Space Physics*, 107(A12):SIA 15–1–SIA 15–16, 2002.
- A. D. Pierce. *Acoustics: An Introduction to Its Physical Principles and Applications*. Acoustical Society of America, 1989.
- A. D. Pierce and S. C. Coroniti. A mechanism for the generation of acoustic gravity waves during thunderstorm formation. *Nature Publishing Group*, 210:1209–1210, June 1966.

- W. E. Potter, D. C. Kayser, and Mauersberger K. Direct measurements of neutral wave characteristics in the thermosphere. *Journal of Geophysical Research*, 81(28): 5002–5012, 1976.
- M. H. Rees. *Physics and Chemistry of the Upper Atmosphere*. Cambridge University Press, 1989.
- P. L. Roe. Approximate riemann solvers, parameter vectors, and difference schemes. *Journal of Computational Physics*, 43:357–372, March 1981.
- R. V. Row. Evidence of long-period acoustic-gravity waves launched into the f region by the alaskan earthquake of march 28, 1964. *Journal of Geophysical Research*, 71(1):343–345, January 1966.
- R. Sabatini, O. Marsden, C. Bailly, and C. Bogey. A numerical study of nonlinear infrasound propagation in a windy atmosphere. *The Journal of the Acoustical Society of America*, 140(1):641–656, August 2016.
- M. L. Salby. *Physics of the Atmosphere and Climate*. Cambridge University Pres, 2012.
- J. F. Scott, P. Blanc-Benon, and O. Gainville. Weakly nonlinear propagation of small-wavelength, impulsive acoustic waves in a general atmosphere. *Wave Motion*, 72: 41–61, January 2017.
- J. B. Snively and V. P. Pasko. Nexcitation of ducted gravity waves in the lower thermosphere by tropospheric sources. *Journal of Geophysical Research*, 113(A060303): 1–21, January 2008.
- G. A. Sod. A survey of several finite difference methods for systems of nonlinear hyperbolic conservation laws. *Journal of Computational Physics*, 27(1):1–31, April 1978.
- W. Stoffregen. Ionospheric effects observed in connection with nuclear explosions at novaya zemlya on 23 and 30 october 1961. *FOAS-Rept A517, Res. Inst. National Defense*, May 1962.

- Louis C. Sutherland and Henry E. Bass. Atmospheric absorption in the atmosphere up to 160 km. *The Journal of the Acoustical Society of America*, 115(3):1012–1032, 2004.
- P. K. Sweby. High resolution schemes using flux limiters for hyperbolic conservation laws. *Society for Industrial and Applied Mathematics*, 21(5):995–1011, June 1984.
- S.L. Vadas, D. C. Fritts, and M. J. Alexander. Mechanism for the generation of secondary waves in wave breaking regions. *Journal of Geophysical Research: Atmospheres*, 123(5):2605–2627, January 2003.
- B. van Leer. Towards the ultimate conservative difference scheme. *Journal of Computational Physics*, 14:361–370, 1974.
- G. Vigeesh, J. Jackiewicz, and O. Steiner. Internal gravity waves in the magnetized solar atmosphere. i. magnetic field effects. *The Astrophysical Journal*, 835(2), January 2017.
- R. A. Vincent. The dynamics of the mesosphere and lower thermosphere. *Springer*, 2 (2197-4284):4–13, March 2015.
- J. Virieux, N. Garnier, E. Blanc, and J. X. Dessa. Paraxial ray tracing for atmospheric wave propagation. *Geophysical Research Letters*, 31(20):20106–20111, October 2004.
- R. L. Walterscheid and M. P. Hickey. One gas models with height dependent mean molecular weight: Effects on gravity wave propagation. *Journal of Geophysical Research Letters*, 117(A12):28,831–28,239, December 2001.
- R. L. Walterscheid and M. P. Hickey. Gravity wave propagation in a diffusively separated gas: Effects on the total gas. *Geophysical Research Letters*, 117(A05303): 1–11, May 2012.
- R. L. Walterscheid, G. Schubert, and D. G. Brinkman. Acoustic waves in the upper mesosphere and lower thermosphere generated by deep tropical convection. *Journal of Geophysical Research*, 108(A11):1–6, November 2003.

- W. Walterscheid and M. P. Hickey. Acoustic waves generated by gusty flow over hilly terrain. *Journal of Geophysical Research*, 110, October 2005.
- Frank M. White. *Fluid Mechanics*. New York: McGraw-Hill, 2008.
- G. B. Whitham. *Linear and Nonlinear Waves*. Wiley-Interscience, 1999.
- A. F. Wickersham. Identification of acoustic gravity wave modes from ionospheric range time observations. *Journal of Geophysical Research*, 71(19):4551–4555, October 1966.
- K. C. Yeh and C. H. Liu. Acoustic gravity waves in the upper atmosphere. *Journal of Geophysical Research*, 12(2):193–216, May 1974.
- M. D. Zettergren and J. B. Snively. Ionospheric signatures of acoustic waves generated by transient tropospheric forcing. *Geophysical Research Letters*, 40(2):5345–5349, October 2013.
- M. D. Zettergren and J. B. Snively. Ionospheric response to infrasonic acoustic waves generated by natural hazard events. *Journal of Geophysical Research*, 120(9):8002–8024, September 2015.
- M. D. Zettergren, J. B. Snively, A. Kmojathy, and O. P. Verkhoglyadova. Nonlinear ionospheric responses to large amplitude infrasonic acoustic waves generated by undersea earthquakes. *Journal of Geophysical Research*, 122(2):2272–2291, January 2017.

Appendix A

DERIVATIONS

A.1 Jacobian: Euler Equations

This is a demonstration of the derivation of the \mathbf{A} matrix in the quasilinear form of the Euler equations, for which characteristics will be obtained. These steps closely follow the derivations of LeVeque [2002]. Start with:

$$\begin{pmatrix} \rho \\ \rho u \\ E \end{pmatrix}_t + \begin{pmatrix} \rho u \\ \rho u^2 + p \\ u(E + p) \end{pmatrix}_x = 0,$$

and an ideal gas equation of state and the definition of energy:

$$E = \frac{p}{\gamma - 1} + \frac{1}{2}\rho u^2.$$

Now, expand the Euler Equations

$$\begin{aligned} \rho_t + (\rho u)_x &= 0, \\ (\rho u)_t + \rho_x u^2 + 2\rho u u_x + p_x &= 0, \\ E_t + u(E_x + p_x) + u_x(E + p) &= 0. \end{aligned}$$

Note:

$$p = E(\gamma - 1) + \frac{1}{2}\rho u^2(1 - \gamma) = 0,$$

$$p_x = E_x(\gamma - 1) + \frac{1 - \gamma}{2}\rho_x u^2 + (1 - \gamma)\rho u u_x = 0.$$

The mass conservation equation stays the same. The momentum, and equation are updated

$$(\rho u)_t + \rho_x u^2 + 2\rho u u_x + E_t(\gamma - 1) + \frac{1 - \gamma}{2}\rho_x u^2 + (1 - \gamma)\rho u u_x = 0,$$

$$E_t + u \left(E_x + E_x(\gamma - 1) + \frac{1 - \gamma}{2}\rho_x u^2 + (1 - \gamma)\rho u u_x \right) + u_x (E + p) = 0.$$

Grouping like terms, the Euler Equations in terms of the EOS are written as:

$$\rho_t + (\rho u)_x = 0,$$

$$(\rho u)_t + \frac{3 - \gamma}{2}u^2 \rho_x + (3 - \gamma)u \rho u_x + (\gamma - 1)E_x = 0,$$

$$E_t + \frac{1 - \gamma}{2}u^3 \rho_x + \left(\frac{E + p}{\rho} + (1 - \gamma)u^2 \right) \rho u_x + \gamma u E_x = 0.$$

Note:

$$H = \frac{E + p}{\rho},$$

So that:

$$\rho_t + (\rho u)_x = 0$$

$$(\rho u)_t + \frac{3 - \gamma}{2}u^2 \rho_x + (3 - \gamma)u \rho u_x + (\gamma - 1)E_x = 0,$$

$$E_t + \frac{1 - \gamma}{2}u^3 \rho_x + (H - (\gamma - 1)u^2) \rho u_x + \gamma u E_x = 0.$$

Make note of

$$\begin{aligned}(\rho u)_x &= \rho_x u + \rho u_x, \\ \rho u_x &= (\rho u)_x - \rho_x u.\end{aligned}$$

Into the above

$$\begin{aligned}\rho_t + (\rho u)_x &= 0 \\ (\rho u)_t + \frac{3-\gamma}{2}u^2\rho_x + (3-\gamma)u[(\rho u)_x - \rho_x u] + (\gamma-1)E_x &= 0, \\ E_t + \frac{1-\gamma}{2}u^3\rho_x + (H - (\gamma-1)u^2)[(\rho u)_x - \rho_x u] + \gamma u E_x &= 0.\end{aligned}$$

Grouping the like terms together again gives: Into the above

$$\begin{aligned}\rho_t + (\rho u)_x &= 0, \\ (\rho u)_t + \frac{\gamma-3}{2}u^2\rho_x + (3-\gamma)u(\rho u)_x + (\gamma-1)E_x &= 0, \\ E_t + \left[\frac{\gamma-1}{2}u^3 - uH \right] \rho_x + (H - (\gamma-1)u^2)(\rho u)_x + \gamma u E_x &= 0.\end{aligned}$$

In matrix form:

$$A = \begin{bmatrix} 0 & 1 & 0 \\ \frac{1}{2}(\gamma-3)u^2 & (3-\gamma)u & \gamma-1 \\ \frac{1}{2}(\gamma-1)u^3 - uH & H - (\gamma-1)u^2 & \gamma u \end{bmatrix}. \quad (\text{A.1})$$

$$\begin{pmatrix} \rho \\ \rho u \\ E \end{pmatrix}_t + A \begin{pmatrix} \rho \\ \rho u \\ E \end{pmatrix}_x = 0. \quad (\text{A.2})$$

The eigenvalues of A are:

$$\lambda = [u - c, u, u + c]^T. \quad (\text{A.3})$$

The coefficients a_1 , a_2 and a_3 are found through noting that

$$a = R^{-1}(q_r - q_l) = R^{-1}\Delta \quad (\text{A.4})$$

where R is the eigenvector matrix $[r^1, r^2, r^3]$. The inverse is computed in Mathematica, and the multiplication is shown below

$$R = \begin{bmatrix} 1 & 1 & 1 \\ u - c & u & u + c \\ H - uc & u^2/2 & H + uc \end{bmatrix}, \quad (\text{A.5})$$

The value for a can be determined

$$a = R^{-1}\Delta = R^{-1} \begin{bmatrix} \rho_l - \rho_r \\ (\rho u)_l - (\rho u)_r \\ E_l - E_r \end{bmatrix}. \quad (\text{A.6})$$

From this, the value for the "waves" are:

$$\mathcal{W}_i = r_i a_i, \quad (\text{A.7})$$

$$a_1 r_1 = \begin{bmatrix} a_1 \\ a_1(u - c) \\ a_1(H - uc) \end{bmatrix} \quad a_2 r_2 = \begin{bmatrix} a_2 \\ a_2 u \\ a_2 u^2/2 \end{bmatrix} \quad a_3 r_3 = \begin{bmatrix} a_3 \\ a_3(u + c) \\ a_3(H + uc) \end{bmatrix}. \quad (\text{A.8})$$

So that the coefficients go as follows:

$$a_2 = \ell, \quad (\text{A.9})$$

$$a_3 = \frac{1}{2c} (\Delta_2 + (c - u)\Delta_1 - ca_2), \quad (\text{A.10})$$

$$a_1 = \Delta_1 - a_2 - a_3, \quad (\text{A.11})$$

$$\ell = \frac{\gamma - 1}{c^2} [(H - u^2) \Delta_1 + u\Delta_2 - \Delta_3]. \quad (\text{A.12})$$

Non-conservative Mass Fraction Density

Consider the advected non-conservative mass-fraction density Y equation

$$Y_t + uY_x = 0. \quad (\text{A.13})$$

Which is already in the form for finding the Jacobian. The coefficient added is u towards the end which gives the following matrix

$$A = \begin{bmatrix} 0 & 1 & 0 & 0 \\ \frac{1}{2}(\gamma - 3)u^2 & (3 - \gamma)u & \gamma - 1 & 0 \\ \frac{1}{2}(\gamma - 1)u^3 - uH & H - (\gamma - 1)u^2 & \gamma u & 0 \\ 0 & 0 & 0 & u \end{bmatrix}. \quad (\text{A.14})$$

Update Equation A.2

$$\begin{pmatrix} \rho \\ \rho u \\ E \\ Y \end{pmatrix}_t + A \begin{pmatrix} \rho \\ \rho u \\ E \\ Y \end{pmatrix}_x = 0. \quad (\text{A.15})$$

Since the non-conservative method is not coupled with the state vector, the eigenvalues and eigenvectors found in Equation A.3-A.5 are not affected by the additional Y

term. The values of a remain the same except for a_4 :

$$a_4 = \Delta_4. \tag{A.16}$$

The coefficients obtained from this derivation describe the values for the "wave" method, which depends on the differences between q_L and q_R to calculate a . The f-wave method used by CLAWPACK depends on the flux differences to obtain the β coefficients. The coefficients from the "wave" method and f-wave method are related through the wave speed

$$\beta_{i-1/2} = s_{i-1/2} a_{i-1/2}. \tag{A.17}$$

In the solver, the β coefficients are recovered automatically after solving from the flux difference (as opposed to difference in q). For the mass-fraction advection, the resulting f-wave is $\mathcal{Z} = s(\Delta_4)$.